MESOSCOPIC SUPERCONDUCTING TUNNEL JUNCTION DEVICES

Experimental Studies of Performance Limitations

Doctoral Dissertation

Jani Kivioja

Helsinki University of Technology
Department of Engineering Physics and Mathematics
Low Temperature Laboratory

MESOSCOPIC SUPERCONDUCTING TUNNEL JUNCTION DEVICES

Experimental Studies of Performance Limitations

Doctoral Dissertation

Jani Kivioja

Dissertation for the degree of Doctor of Science in Technology to be presented with due permission of the Department of Engineering Physics and Mathematics for public examination and debate in Auditorium F1 at Helsinki University of Technology (Espoo, Finland) on the 9th of June, 2005, at 12 noon.

Helsinki University of Technology
Department of Engineering Physics and Mathematics
Low Temperature Laboratory

Teknillinen korkeakoulu
Teknillisen fysiikan ja matematiikan osasto
Kylmälaboratorio

HELSINKI UNIVERSITY OF TECHNOLOGY	ABSTRACT OF DOCTORAL DISSERTATION
P.O. BOX 1000, FI-02015 TKK	
http://www.tkk.fi	

Author

Name of the dissertation

Date of manuscript	Date of the dissertation
Monograph	Article dissertation (summary + original articles)

Department	
Laboratory	
Field of research	
Opponent(s)	
Supervisor	
(Instructor)	

Abstract

Keywords

Number of pages	ISBN (printed)
ISBN (pdf)	ISBN (others)
ISSN (printed)	ISSN (pdf)

Publisher

Print distribution
The dissertation can be read at http://lib.tkk.fi/Diss/

Preface

The work reviewed in this Thesis has been carried out at the Department of Physics in the University of Jyväskylä during the years 2001-2002 and in the Low Temperature Laboratory at the Helsinki University of Technology from beginning of 2003 until now.

I would like to express my gratitude to my supervisor Academy Professor Jukka Pekola. His skill to establish such a special enthusiastic atmosphere is irreplaceable as is his wisdom and his persistent guidance. I would also like to thank Dr. Ilari Maasilta for his supervising and practical help in the beginning of my work. I am grateful to Prof. Mikko Paalanen, Prof. Frank Hekking, Prof. Olivier Buisson and Prof. Pertti Hakonen for their advice, support and those fruitful discussions. I also wish to thank Dr. Alexandre Savin for his diligent support.

The atmosphere of the SOFY and the PICO research groups has been inspiring and I was honored to get numerous valuable friends for the rest of my life. Especially I would like to thank my dear "roommate" Dr. Jussi Toppari for those long days and nights with our new measuring setup in the LTL and for his persistent work with the Cooper pair pumps, Dr. Antti Niskanen for those educating and fun moments during sluice measurements, M.Sc. Lasse Taskinen and M.Sc. Jenni Karvonen for their continuing work on SINIS structures, M.Sc. Tommi Nieminen for making those outstanding junctions and also for his work on the noise experiment and Dr. Arttu Luukanen for being such an inspiring friend.

I also would like to thank Dr. Tero T. Heikkilä for instructive theoretical advice and discussions. I have also greatly benefited from working with talented and excellent fellow graduate and undergraduate students: Antti Finne, Jouni Flyktman, Kimmo Kinnunen, Pasi Kivinen, Panu Koppinen, Rene Lindell, Antti Nuottajärvi, Teemu Ojanen, Leif Roschier, Mika Sillanpää and Tarmo Suppula. The staff in the LTL and at the Department of Physics in the University of Jyväskylä have been exceptional and they also

deserve my acknowledgments.

Most of all I wish to thank my wife Maarit for her love and support during these years.

Espoo, June 2005

Jani Miikkael Kivioja

Contents

Appended papers

This Thesis consists of a review section and the following original publications:

DETECTION OF CURRENT BY A JOSEPHSON JUNCTION

[**PI**] J.M. Kivioja, T.E. Nieminen, J. Claudon, O. Buisson, F.W.J. Hekking, and J.P. Pekola, *Observation of transition from escape dynamics to underdamped phase diffusion in a Josephson junction*, accepted for publication in Physical Review Letters (2005); cond-mat/0501383 (2005).

[**PII**] J.M. Kivioja, T.E. Nieminen, J. Claudon, O. Buisson, F.W.J. Hekking, and J.P. Pekola, *Weak coupling Josephson junction as a current probe: effect of dissipation on escape dynamics*, submitted to New Journal of Physics (2005).

[**PIII**] J.P. Pekola, T.E. Nieminen, M. Meschke, J.M. Kivioja, A.O. Niskanen, and J.J. Vartiainen, *Shot-noise-driven escape in hysteretic Josephson junctions*, submitted to Physical Review Letters (2005); cond-mat/0502446 (2005).

COOPER PAIR PUMP

[**PIV**] J.J. Toppari, J.M. Kivioja, J.P.Pekola, and M.T. Savolainen, *Turnstile Behaviour of the Cooper Pair Pump*, Journal of Low Temperature Physics **136**, 57 (2004).

[**PV**] A.O. Niskanen, J.M. Kivioja, H. Seppä, and J.P.Pekola, *Evidence of Cooper-pair pumping with combined flux and voltage control*, Physical Review B **71**, 012513 (2005).

THERMOMETRY BASED ON NIS TUNNEL JUNCTIONS

[**PVI**] J.M. Kivioja, I.J. Maasilta, J.P. Pekola, and J.T. Karvonen, *Response time of a thermometer based on normal metal - insulator - superconductor (NIS) tunnel junctions*, Physica E **18**, 21 (2003).

[**PVII**] L.J. Taskinen, J.M. Kivioja, J.T. Karvonen, and I.J. Maasilta, *Direct measurements of the electron-phonon relaxation rate in thin copper films*, phys. stat. sol (c) **11**, 2856 (2004).

In the following chapters the above articles are referred as [PI]-[PVII].

Author's contribution

The work reported in this thesis was partly performed in the Laboratory of Applied Physics at the University of Jyväskylä in years 2001 and 2002 [PVI,PVII], but majority of the research was carried out in the PICO group in the Low Temperature laboratory (LTL) at Helsinki University of Technology between years 2002 and 2005 [PI-PV].

In year 2001, the author built the experimental setup including the dilution refrigerator for the measurements in articles [PVI] and [PVII]. The author partly took care of sample fabrication for experiments in publication [PVI]. The PICO group was founded at the end of year 2002 and the author was taking mainly care of the design and construction of the experimental setup in LTL. The author also constructed and renovated the dilution refrigerator system with high frequency lines used in [PIV], [PV] and partly in [PI] and [PII] together with the first author of [PIV].

The author of this Thesis has written the publications [PI, PII, PVI] and partly the publication [PIV]. The author has taken mainly care of the measurements, analyzed the data and developed the models for Publications [PI], [PII] and [PVI]. Part of the measurements of publications [PI] and [PII] were performed in Grenoble, France, in CRTBT laboratory of the C.N.R.S, in which the author also participated. The measurements for [PIV] and [PV] were performed by the author together with the first author of these publications. In [PV] the experimental details excluding sample fabrication have been taken care by the author. In [PIII] the author has participated in measurements and data analysis.

The author has presented results of this Thesis in a number of international conferences and workshops including: the 2nd International School

for Young Scientists and the 5th International Workshop *"From Andreev Reflection to the International Space Station"* in Björkliden, Kiruna, Sweden, (2001), the 3rd International School for Young Scientists and the 6th International Workshop *"From Andreev Reflection to the International Space Station"* in Björkliden, Kiruna, Sweden (2002), *the 23rd International Conference on Low Temperature Physics* (LT23), Hiroshima, Japan (2002), *Conference on Precision Electromagnetic Measurements* (CPEM 2004), London, England (2004), and *Frontiers of Quantum and Mesoscopic Thermodynamics* (FQMT 2004), Prague, Czech Republic (2004).

Chapter 1

Introduction

The present high tech electronics, *e.g.*, mobile technology, are mainly based on Maxwell's equations presented at the end of the 19$^{\text{th}}$ century. These equations in addition to Newtonian mechanics are capable of explaining mostly our macroscopic word. However, we do already have individual applications, *e.g.*, Schottky tunneling diode [1], whose basic operation could not be understood without quantum mechanics [2]. Till now, the everyday electronics have not incorporated the advantages provided by quantum mechanics in large scale, but it is clear that the development tends towards quantum nature. Firstly, smaller and smaller structures of the integrated circuit technology [3] are pushing one to take quantum phenomena into account and on the other hand, the needs of some new research fields, *e.g.*, quantum information technology [4], can not be fulfilled by classical electronics.

Four different mesoscopic[1] superconducting devices have been experimentally studied in this Thesis. These devices make use of phenomena related to superconductivity [5] and are also benefiting from some properties of small structures, *e.g.*, of quantum mechanical tunneling and of transport of single electrons [6]. The present research focused on investigating performance limitations of these devices and the aim was to improve their performance. The work was mainly experimental and the measurements were carried out at millikelvin temperatures. All the experimental setups were built during this Thesis work.

This Thesis is organized as follows. First a brief theoretical background is given in Chapter 2. In Chapters 3, 4, and 5 the main results on studied devices are presented. Chapter 3 is dedicated to the results of the ammeter, based on a hysteretic Josephson junction switching from the superconducting state to the normal state [PI, PII]. One aim of these studies was to increase

---

[1]mesoscopic=intermediate regime between macroscopic and microscopic

the sensitivity of the current detection. In this Chapter we also see an example, where a Josephson junction is used as a shot noise detector [PIII] . The topic of Chapter 4 is Cooper pair pumping. This Chapter presents two different devices: the beginning of the chapter describes a conventional Cooper pair pump based on two superconducting islands separated by tunnel junctions [PIV] . After this, observations on a novel flux assisted Cooper pair pump [PV] are presented. Chapter 5 discusses the limitations on the speed of a thermometer, which is based on a tunnel junction between a superconductor and a normal metal (Publications [PVI] and [PVII]). Finally Chapter 6 concludes this Thesis.

Chapter 2

A mesoscopic superconducting tunnel junction

A *tunnel junction* consists of an insulating layer between conducting electrodes. A thin enough barrier permits electrons to tunnel quantum mechanically through. In the case of metallic electrodes, the conductors can be either in normal or in superconducting state, which strongly influences the dynamics of the junction. Furthermore, the behaviour is dependent on the physical size of the junction. This Chapter gives a short review of mesoscopic tunnel junctions, where at least one of the electrodes is superconducting. A more detailed view of tunneling of single electrons can be found, *e.g.*, in Ref. [6] and a general introduction to superconductivity is given, *e.g.*, in Ref. [5].

2.1 Small tunnel junctions and Coulomb blockade

In the single electron tunneling devices tunneling is controlled by the charging energy of individual electrons across a junction. In particular, tunneling can be suppressed by this charging energy, which is the phenomenon called *Coulomb blockade*. The tunnel junction, two conducting electrodes separated by a thin insulating layer, is a capacitor as well. Tunneling of one electron across the junction changes the electrostatic energy by an amount

$$\Delta E = \frac{1}{2}\frac{(Q-e)^2}{C_J} - \frac{1}{2}\frac{Q^2}{C_J}, \tag{2.1}$$

where C_J is the junction capacitance, $Q = VC_J$ is the initial charge and e is the elementary charge. With applied bias voltages of $V < e/2C_J$, the energy difference is positive and the tunneling event is thus energetically

forbidden in the low temperature limit. This leads to a vanishing tunneling current despite of a non-zero bias voltage and this is a simple example of the Coulomb blockade phenomenon.

Both thermal and quantum fluctuations can smear out the single electron effects and this sets constraints in single electron tunneling experiments. The condition for Coulomb blockade to exist is that the charging energy of a single electron, $E_C = e^2/2C_J$, is larger than the energy fluctuations. Thermal fluctuations give the constraint that E_C must exceed $k_{\mathrm{B}}T$. This limits the size of a tunnel junction into mesoscopic scales and also pushes the measuring temperatures down. For example, the required junction capacitance is of the order of 10^{-18} F = 1 aF at room temperature which is, unfortunately, far beyond the reach of the present technology. Nowadays the smallest tunnel junction size achieved routinely is somewhat below $\approx$100x100 (nm)^2. For an $AlOx$ tunnel barrier, this yields junction capacitance of the order of 0.5 fF, which limits the measuring temperatures to values well below 1 K.

The other condition is given by quantum fluctuations, where the quantum energy uncertainty $\Delta E \geq h/\Delta t \approx h/RC_J$, associated with the finite lifetime of the charge on the capacitor must be smaller than E_C [5]. Here R is the shunting impedance seen by a tunnel junction. Equating E_C to ΔE gives the requirement that R must be larger than the quantum resistance $R_K = h/e^2 \approx 26$ $k\Omega$. This limit is hard to fulfill in the case of single junction devices, because the relevant impedance is usually given by the high frequency properties of the measuring leads, which yields an impedance which is of the order of vacuum impedance $Z_0 = \sqrt{\mu_0/\epsilon_0} \approx 377$ Ω. However, in the devices which contain more than one junction in series, *e.g.*, in a single electron transistor described below, the requirement is easily met and it limits the tunnel junction resistances R_T to values larger than R_q. In this case the single electron effects are clearly observable as long as the requirement given by the thermal fluctuations is met.

In a single electron transistor (SET) one is able to control the charge of a mesoscopic island or grain within the accuracy of e. A SET is schematically presented in Fig. 2.1 (a). It consists of a single island, which is connected to biasing electrodes via ultra small tunnel junctions and a gate electrode, which is capacitively coupled to the island with capacitance C_g. One can store a part of the charge into this gate capacitance and hence "tune" the Coulomb blockade by gate voltage V_g. The energy of SET under zero bias voltage V can be written as

$$E_{ch} = \frac{1}{2}\frac{e^2}{C_\Sigma}(V_g C_g/e - n)^2 \quad (+constant), \tag{2.2}$$

where $C_\Sigma = 2C_J + C_g$ is the sum of all island capacitances and n is the
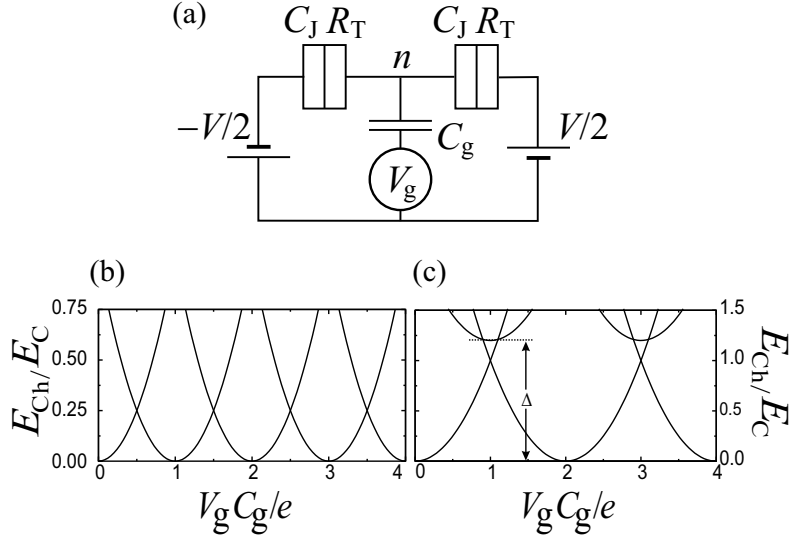
Figure 2.1: (a) The schematic of a single electron transistor (SET). The single island is connected to electrodes by tunnel junctions with capacitance C_J and normal state resistance R_T. (b) The charging energy of a single electron transistor as a function of V_g consists of a set of parabolas, each corresponding to a certain number n of the extra electrons on the island. (c) The charging energy of a superconducting SET (SSET). In the case $\Delta > E_C$, the periodicity of SSET is $2e$. Each minimum corresponds to an integer number of *Cooper pairs* on the island.

number of electrons *added* to the island from initial neutral condition. Here, symmetric junctions and negligible self capacitance of the island are assumed. Figure 2.1 (b) presents the charging energy as a function of gate charge in units of $E_C = \frac{1}{2}\frac{e^2}{C_\Sigma}$. It consists of a set of parabolas, each corresponding to an integer number of excess electrons on the island. At the degeneracy point $V_g C_g/e = n + 1/2$ different parabolas cross and thus at each of these points the number of electrons on the island changes by $\pm$ *one* when sweeping V_g.

A single electron transistor can also be made to be superconducting. In superconducting SETs (SSET), the charge carriers are either Cooper pairs or quasiparticles (electrons). If the total number of conduction electrons on the island is even, all electrons can be paired, but if this number is odd, the energy of one electron must be above the superconducting gap $\Delta_{BCS} = 1.764\,k_\mathrm{B}T_c$ [5]. Here T_c is the critical temperature of the superconductor. The energy of the odd charge states are thus lifted and in the case $E_C < \Delta_{BCS}$, the gate charge periodicity is $2e$, as presented in Fig. 2.1 (c). Another condition of this *parity effect* is given by thermal excitations of quasiparticles on the island,

which limits the measuring temperature to below $T^* = \Delta_{BCS}/k_{\mathrm{B}} \ln\left(N_{eff}\right)$ [7]. Here N_{eff} is the total number of quasiparticle states within $k_{\mathrm{B}}T$ above the superconducting gap on the island. It is typically of the order of 10^4 for small island volumes [5], which means that the temperature condition can be written as $T^* \approx T_c/5$. For aluminum samples, $T_c \approx 1.2$ K, this is around 240 mK. Also high frequency noise can produce quasiparticles and cause parity changes, $e.g.$, either by heating the sample above T^* or by directly exciting quasiparticles if the frequency is above $2\Delta_{BCS}/h$.

2.2 SIS tunnel junction

2.2.1 Josephson effects

The Superconductor - Insulator - Superconductor (SIS) tunnel junction is a Josephson junction similar to other superconducting weak links. The phenomenological Ginzburg-Landau theory describes superconductivity by complex macroscopic wavefunctions $\psi(\vec{r}) = |\psi(\vec{r})|e^{i\phi(\vec{r})}$, which represent the local density of superconducting electrons $n_s(r) = |\psi(\vec{r})|^2$ [5]. Here a real function $\phi(\vec{r})$ defines the phase of the wavefunction. In a Josephson junction (JJ), these macroscopic wavefunctions of the superconducting electrodes overlap and therefore the junction is able to carry supercurrent. The supercurrent through the JJ is given by the so-called dc $Josephson$ $relation$

$$I = I_c \sin(\varphi). \qquad (2.3)$$

Here, I_c is the critical current of the junction, $i.e.$, the maximum supercurrent that the junction can support, and $\varphi = \phi_i - \phi_j$ is the phase difference between the wavefunctions of the different electrodes. The critical current can be related to the normal state tunneling resistance R_T through the Ambegaokar-Baratoff formula [5, 8]

$$I_c = (\pi\Delta_{BCS}/2eR_T)\tanh\left(\Delta_{BCS}/2k_{\mathrm{B}}T\right), \qquad (2.4)$$

where T is the temperature of the superconductor. The ac $Josephson$ $relation$ reads

$$2eV = \hbar\frac{d\varphi}{dt}, \qquad (2.5)$$

which connects the voltage across the junction to the time derivative of the phase. This implies that the dc voltage across the junction would produce an alternating current with amplitude of I_c and with frequency of $f = 2eV/h$.
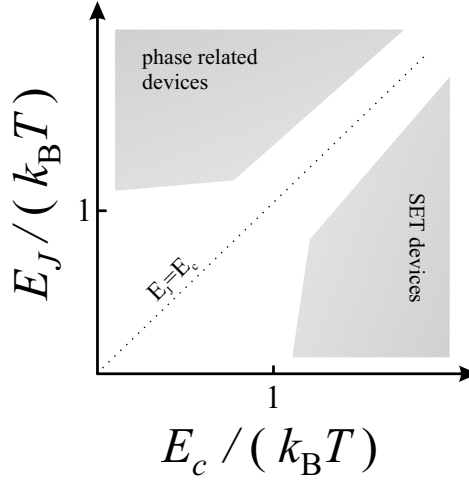
Figure 2.2: Schematical diagram of different regimes of the Josephson junction devices.

2.2.2   Characteristic parameters

The strength of the coupling across a SIS junction can be given by Josephson energy $E_J = \frac{\Phi_0}{2\pi}I_c$. Here $\Phi_0 = h/2e \simeq 2 \cdot 10^{-15}$ Wb is the quantum of the magnetic flux. The total energy includes also a charging energy part $E_C = e^2/2C_J$ as described in Section 2.1. The system is dissipative due to junction shunting resistance $R(\omega) = 1/Re\{Y(\omega)\}$, which has to be taken into account in addition to E_J and E_C for a full Josephson junction characterization. Here $Y(\omega)$ is the admittance of the environment of the Josephson junction at frequency ω.

The characteristic JJ energy parameters are related to different dynamical variables of the system: E_J is related to the phase difference φ and E_C to the charge $Q = ne$. In fact, these two quantities are conjugate variables, which yields the quantum uncertainty relation $\Delta\varphi\Delta n \geq 1$. If the capacitance of the junction is large, i.e. $E_C \ll E_J$, the phase fluctuations $\Delta\varphi$ are small and the junction behaves semiclassically. In this limit, the junction can be well described by taking only the Josephson coupling energy into account $[H = H_J = -E_J\cos(\varphi)]$. With decreasing junction size, the charging energy starts to play a role. In the limit, where E_C is comparable with E_J, the coupling energy is not sufficient for the full description of the dynamics and the charging energy should be taken into account as well $[H = H_c + H_J = Q^2/2C - E_J\cos(\varphi)]$. In the opposite extreme $E_C \gg E_J$, the charge is a "good quantum number" and the dynamics are mainly determined by discrete tunneling of Cooper pairs.

Depending on the energy scales, one can roughly separate the Josephson junction applications into the phase related devices, where $E_J \gg E_C$, and into the single charge devices where $E_J < E_C$. In both regimes, the relevant energy must be larger than the thermal energy $k_\mathrm{B}T$, in order to keep phase constant or to avoid thermal fluctuations average over many charge states. Figure 2.2 schematically presents different regimes of Josephson junction devices on the (E_C, E_J)-plane. The phase related devices, *e.g.*, the ammeter presented in Chapter 3, are located in the upper left corner. On contrary, the devices where single charge tunneling is important, *e.g.*, charge pumps presented in Chapter 4, are in the lower right corner.

2.2.3   Basics of a *dc*-SQUID

A *dc*-SQUID consists of two weak links and a superconducting loop. In the limit of small loop inductance L_{loop} ($\beta_L \equiv \frac{2\pi L_{loop} I_c}{\Phi_0} \ll 1$ [5]), the potential energy of the *dc*-SQUID can be written as

$$U_J(\gamma) = E_J\sqrt{2(1+\alpha^2) + 2(1-\alpha^2)\cos(\frac{2\pi\Phi}{\Phi_0})} \ \cos(\gamma), \qquad (2.6)$$

where γ is the phase accross the *dc*-SQUID, Φ is the magnetic flux through the loop and α is an asymmetry parameter of the *dc*-SQUID ($E_{J1,J2} = E_J(1\pm\alpha)$). The supercurrent ($I_{sc} = \frac{2e}{\hbar} \ \partial U_J/\partial\gamma$) can in this case be written as $I = I_c^0\sqrt{2(1+\alpha^2) + 2(1-\alpha^2)\cos(\frac{2\pi\Phi}{\Phi_0})} \ \sin(\gamma)$. Thus, if $\alpha = 0$, we can write $I = I_c\sin(\gamma)$, where

$$I_c = 2I_c^0|\cos(\pi\Phi/\Phi_0)|. \qquad (2.7)$$

The potential energy of the *dc*-SQUID has also an inductive contribution due to the inductance of the *dc*-SQUID loop, but if the Josephson inductance $L_J = \Phi_0/2\pi I_c$ is much larger than the loop inductance ($\beta_L \ll 1$), this term is not effecting the dynamics and we can neglect it [9]. In an ideal case, $\alpha = 0$, the *dc*-SQUID is a tunable single junction with a twice higher maximum critical current compared to one junction in the loop.

2.3   NIS tunnel junction

The behaviour of the NIS (Normal metal - Insulator - Superconductor) tunnel junction differs from that of the SIS junctions fundamentally, and also from that of NIN junctions (Normal metal - Insulator - Normal metal). Because one of the electrodes is in the normal state, NIS junctions are not able to carry supercurrent and thus, *e.g.*, the Josephson effect is not present. However, the

superconducting gap on one side of the junction yields a negligible tunneling rate at voltages below Δ/e.

The net current through the NIS junction is

$$
\begin{aligned}
I(V) &= I_{N \to S} - I_{S \to N} \\
&= A \int_{-\infty}^{\infty} N_N(E - eV)N_S(E)[f(E, T_S) - f(E - eV, T_e)]dE,
\end{aligned}
\tag{2.8}
$$

where $f(E, T)$ is the Fermi-function and A is the tunneling coefficient, which is assumed to be constant over the energies of interest. The electronic temperatures are given by T_e and T_S in the normal metal and in the superconducting side, respectively. N_N is the density of states in the normal metal, which is approximately constant near the Fermi energy, and the density of states in the superconductor is given by

$$
N_S(E) = N_N(E) \times \left\{ \begin{array}{ll} \frac{|E|}{\sqrt{E^2 - \Delta^2}} & , |E| > \Delta \\ 0 & , |E| < \Delta \end{array} \right. .
\tag{2.9}
$$

By approximating $N_N(E) \approx N_N(0)$, we can write the tunneling current into the form

$$
I(V) = \frac{1}{eR_T} \int_{\Delta}^{\infty} \frac{|E|}{\sqrt{E^2 - \Delta^2}}[f(E - eV, T_e) - f(E + eV, T_e)]dE,
\tag{2.10}
$$

where $R_T = [AeN_N(0)N_N(0)]^{-1}$. Note that $I(V)$ in Eq. (2.10) is independent of the superconductor temperature. At $T_e = 0$, the tunneling current is zero at voltages below the superconducting gap ($V < \Delta/e$). Above this, the current has the form $I = \sqrt{V^2 - (\Delta/e)^2}/R_T$, which is asymptotically approaching the NIN junction result $I = V/R_T$ with increasing voltage.

With increasing temperature the voltage threshold at Δ/e becomes increasingly rounded. In the case $k_B T_e \ll \Delta$ and $0 \ll eV < \Delta$, the $I(V)$ can be approximately written as [10]

$$
I(V) \simeq I_0 \, e^{(eV - \Delta)/k_B T_e},
\tag{2.11}
$$

where $I_0 = \frac{\Delta}{eR_T}\sqrt{\frac{\pi k_B T_e}{2\Delta}}$.

2.4   Fabrication of mesoscopic tunnel junctions

All samples used in the experiments were fabricated by standard electron beam lithography and shadow angle evaporation [11]. A fabrication process

is briefly the following: A thin PMMA/PMMA-MAA bilayer resist with a thickness around 500 nm was spun over the oxidized silicon substrate. The resist layer was patterned by *electron beam lithography* using a scanning electron microscope (SEM). Next, in the *developing process*, the exposed resist areas were removed using methyl isobutyl ketone:isopropyl alcohol (1:3) solution. Then, thin films of metal were *evaporated* in an ultra high vacuum chamber. The insulating *AlOx* layer for the tunnel junctions was formed by basic room temperature oxidation between the evaporation of different metal layers. Finally, in the *lift-off* process, the remaining resist together with the extra metal film on top of it, was removed in a acetone bath.

Chapter 3

Josephson junction ammeter

A hysteretic Josephson junction switching from zero to a non-zero voltage state can be used as a current threshold detector. Recently in many superconducting quantum bit experiments this phenomenon has successfully been used in the detection of the quantum state [12,13]. Switching measurements also allow one to perform conventional large bandwidth current measurements, and there have been proposals to use it as a classical *ammeter* for studying phenomena like shot noise [14,15].

For many purposes, a smaller critical current I_c of the detecting junction would yield a higher current sensitivity. Yet the physics governing escape phenomena of small I_c junctions, *i.e.*, junctions where the thermal energy $k_{\mathrm{B}}T$ is significant as compared to the Josephson coupling energy $E_J = \frac{\hbar}{2e}I_c$, ultimately differs from those with larger I_c [16,17,18]. This work investigates experimentally how far one can reduce I_c still maintaining the useful features of the detector.

3.1   RCSJ model

The dynamics of the Josephson junction in a phase related regime ($E_J \gg E_c$) can be described by the RCSJ model (Resistively and Capacitively Shunted Junction). In this model, the tunnel junction is considered as a parallel combination of an ideal Josephson junction, a junction capacitance C_J and a dissipative impedance $R(\omega)$. The model circuit is presented with solid black lines in the inset of the Fig. 3.1. The model yields a picture, where a fictive phase particle (phase φ) of mass $m = \hbar^2/8E_C$ resides in a tilted cosine potential

$$U(\varphi) = -E_J \left[\cos(\varphi) + I/I_c \; \varphi\right], \qquad (3.1)$$

schematically presented in Fig. 3.1. Here I is the biasing current. The motion of φ is affected also by a viscous drag force $(\frac{\hbar}{2e})^2 \ 1/R \ \frac{d\varphi}{dt} = Q^{-1}\frac{d\varphi}{dt}$, where $Q = \omega_p R(\omega) C_J$ is the quality factor of the junction. Here, $\omega_p = \sqrt{\frac{d^2U/d\varphi^2}{m}} = \frac{1}{\hbar}\sqrt{8E_J E_C} \ q_0^{1/2}$ is the plasma frequency, *i.e.*, the angular frequency of small oscillations around the metastable minimum of the potential, and $q_0 \cong \sqrt{2(1 - I/I_c)}$. When the biasing current is close to the critical value, the potential is well approximated by the cubic potential

$$U(q) = 3 \ \Delta U \ (q/q_0)^2[1 - \frac{2}{3}(q/q_0)], \tag{3.2}$$

where $q = \varphi/2 - \frac{\pi}{4} + \frac{1}{2}q_0$, and $\Delta U = \frac{2}{3} \ E_J \ q_0^3$ is the height of the potential barrier.

3.1.1   Dynamics of a Josephson junction

The dynamics of the Josephson junction can be either overdamped ($Q < 1$) or underdamped ($Q > 1$). In the underdamped dynamics the IV-characteristic of the junction is hysteretic: with increasing current the voltage will jump abruptly from zero (or almost) to $V \approx 2\Delta_{BCS}/e$ at $I = I_{sw} < I_c$. On the contrary, in the case $Q < 1$ the IV-characteristic is non-hysteretic and the voltage increases continuously. Note however, that the frequency dependent Q can lead to hysteresis although the junction would present overdamped dynamics inside a well, as will be discussed below [19, 20].

Figure 3.1 presents schematically the dynamics of a hysteretic Josephson junction. The upper inset shows an example of a measured IV-characteristic, and the corresponding dynamics of the phase particle in tilted cosine potential has been presented in the main frame. There are two distinguishable states of the system: the superconducting S-state and the high voltage N-state. In the first one, the phase has constant average value and the voltage across the junction is close to zero. With increasing current the phase particle *escapes* from the metastable S-state and switch to the second state, where the phase is running freely. In this N-state the voltage is about twice the superconducting gap ($2\Delta_{BCS}/e \approx 360 \ \mu$V in aluminum). Escape is a fully stochastic phenomenon and the value of the switching current changes from one current sweep to another. With decreasing current, the dissipation is slowing down the phase particle and at $I = I_r$ it will be relocalized again to the S-state. This *retrapping* current I_r differs from that of escaping and it strongly depends on the dissipation.

Phase particle can escape from a metastable well either via thermal activation (TA) over, or macroscopic quantum tunneling (MQT) through the
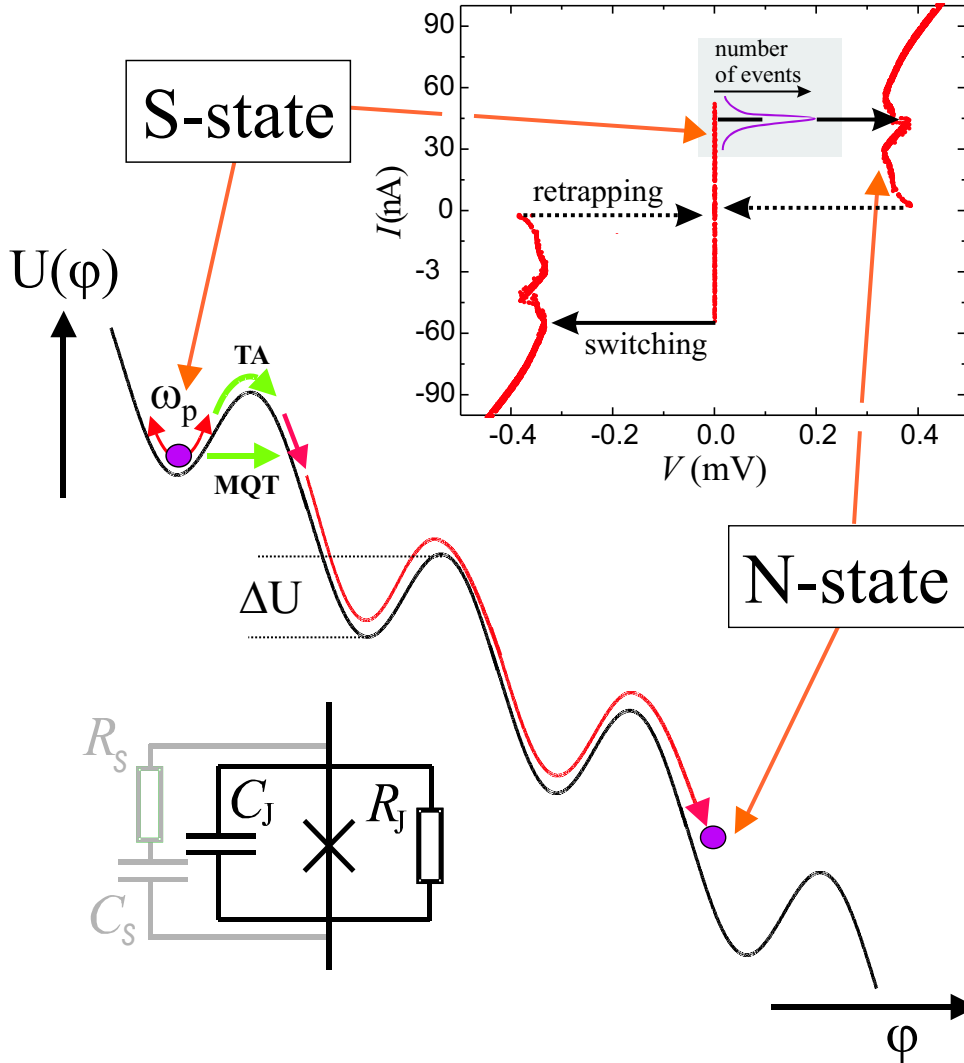
Figure 3.1: Dynamics of a hysteretic Josephson junction. The top frame presents an example of a measured IV-characteristic. The lower left corner presents the schema of the RSCJ-model with frequency independent (black) and frequency dependent (gray) shunting impedance. In the superconducting state (S-state) the phase mainly oscillates in the well and the average voltage is zero. The phase particle can escape from a well either by thermal activation (TA) or by macroscopic quantum tunneling (MQT) and the system switches to the free running state (N-state). In the N-state the voltage across the junction is approximately twice the superconducting gap ($2\Delta_{BCS}/e \approx 360\,\mu$V for aluminum). The escape is a stochastic process and by sweeping the current repeatedly one can measure the distribution of the switching currents (shown schematically in the IV-characteristic figure). In this work we used a pulse technique, which measures an integral of this distribution directly.

barrier. Below the crossover temperature $T_0 = \hbar\omega_p/2\pi k_{\mathrm{B}}$ the dominant mechanism is MQT. For large junctions, $(\hbar\omega_p \ll \Delta U)$ we can assume a continuum of levels within a metastable potential well, which leads to the thermal activation rate

$$\Gamma_{TA} = \frac{\omega_p}{2\pi}\, e^{-\frac{\Delta U}{k_{\mathrm{B}}T}}, \tag{3.3}$$

where ΔU is the height of the potential barrier [21]. The MQT tunneling rate can be calculated using standard WKB approximations leading to [21]

$$\Gamma_{MQT} = 12\sqrt{6\pi}\frac{\omega_p}{2\pi}\sqrt{\frac{\Delta U}{\hbar\omega_p}}e^{-\frac{36}{5}\frac{\Delta U}{\hbar\omega_p}}. \tag{3.4}$$

The total escape rate can be approximated by $\Gamma_{TOT}(I) \simeq \Gamma_{MQT}(I) + \Gamma_{TA}(I)$ and the total escape probability in the time interval $0 \leq t \leq \tau$ can be written as $P = 1 - e^{-\int_0^\tau \Gamma_{TOT}[I(\tau)]dt}$.

The two conventional methods to investigate escape dynamics are as follows: (i) Ramping the bias current through the junction and measuring the distribution of the switching currents, or (ii) measuring the escape rate directly at different values of the bias current. Escape rates per unit time can be determined via the switching probability with a set of current pulses with fixed amplitude and duration, determining the statistical probability of a junction to switch into a high voltage free running state. Usually, one measures the switching probability as a function of current pulse amplitude $P(I)$, which yields *cumulative histograms* of switching currents (see *e.g.* Fig. 3.9).

In a typical experimental setup, the junction is capacitively shunted, besides by the junction capacitance, also by the stray capacitance of, *e.g.*, the leads (presented schematically with gray lines in Fig. 3.1). At low frequencies, the dissipation is mostly determined by the junction subgap resistance R_J, which is usually of the order of 1 MΩ, but at high frequencies, the impedance is typically small, impedance due to C_s is low and R_s is small. In the S-state the phase mainly oscillates in a well at plasma frequency and it may transit from a well to another in a time which is of the order of the inverse plasma frequency. The dissipation is thus characterized by $R(\omega_p)$ in this case. Without specially designed environmental circuit this high frequency dissipation is usually of the order of vacuum impedance $Z_0 = \sqrt{\mu_0/\epsilon_0} \approx 377\,\Omega$. Yet, after escaping to the N-state, the dominant part of dissipation takes place at low frequencies. Hence, the junction can have very large Q at low frequencies with very small retrapping current combined with an overdamped behaviour in the supercurrent branch [19, 20].
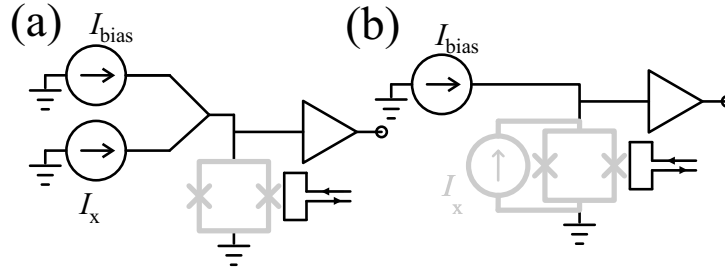
Figure 3.2: Schematical examples of current threshold detection using Josephson junctions or dc-SQUIDs. The thick gray lines indicate the required superconducting parts of the measuring circuits. I_x is the unknown current to be measured and I_{bias} is the biasing current. (a) Circuit for a classical current probing. (b) The unknown circuit is reactive (superconducting) parallel circuit.

3.2 Current threshold detection using Josephson junctions

Schematical examples of circuits used in a current threshold detection are presented in Fig. 3.2 (a) and (b). In these setups, the goal is to measure the current induced by a generic current source. This current is called I_x. The thick lines indicate the superconducting parts of the circuits and the principal difference between circuits shown in (a) and (b) is that the circuit in (a) can be used for measuring currents induced by externally *biased* circuits in contrast to (b), where the measured circuit is purely a reactive parallel circuit and it can be used for measuring a persistent supercurrent. The circuit presented in Fig. 3.2 (a) can be used in a conventional current measurement and it is used, *e.g.*, in studies of shot noise [PIII]. The scheme shown in Fig. 3.2 (b) is similar to what has been used, *e.g.*, in the "Quantronium" experiment [12, 22, 23], but the circuit has also been proposed for measurements of quantum errors in Cooper pair pumping [24]. In both examples, (a) and (b), the measured current I_x runs in parellel with biasing current I_{bias} through the measuring junction (or a dc-SQUID as in Fig. 3.2), and the corresponding change in escape probability is measured. Current measurement scheme is described in more detail in [PII].

The sensitivity of the current threshold detection with constant bias current pulses can be defined as the derivative of the cumulative histogram $S = dP/dI$. The maximum sensitivity is reached with the current pulse amplitude, which corresponds approximately to 70 % switching probability. Figure 3.3 presents the maximum sensitivity as a function of the critical
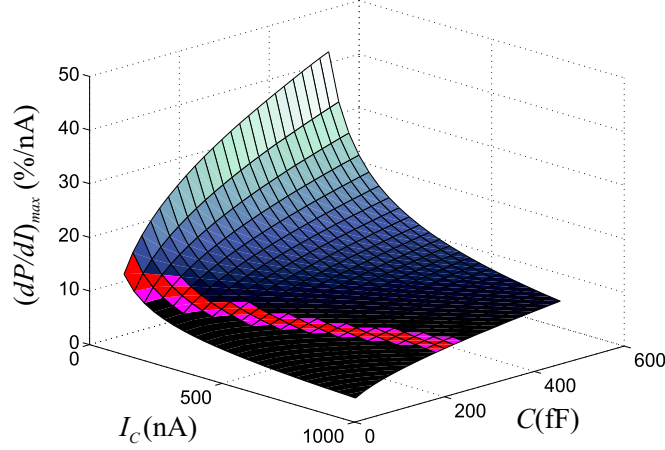
Figure 3.3: The maximum current sensitivity of switching measurements as a function of junctions capacitance and critical current calculated by using TA and MQT models. The red region is indicating the regime of a typical single Al-AlOx-Al tunnel junction.

current and capacitance, calculated by using TA and MQT models. The sensitivity is increasing strongly with decreasing I_c and increasing C_J. It is noteworthy that a single Josephson junction with fixed oxidation parameters is covering only a line on the $(I_c - C)$-plane in Fig. 3.3 with an almost constant sensitivity. This is presented as a lighter region for a typical Al-AlOx-Al tunnel junction. The values used here are $\rho_\square = 1$ k$\Omega(\mu$m$)^2$ for area resistivity ($R_T = \rho_\square/A$) and $c_\square = 50$ fF$/(\mu$m$)^2$ for capacitance per junction area ($C_J = c_\square A$). If one is decreasing the critical current by decreasing the junction area, also the junction capacitance is decreasing and the sensitivity $(dP/dI)_{max}$ remains fixed. Therefore it is beneficial to use a dc-SQUID instead, since one can tune the critical current and capacitance independently and thus increase the sensitivity remarkably.

3.3 Limitations in Josephson junctions with weak coupling

3.3.1 Phase diffusion

In the S-state, the voltage across the junction is not necessarily exactly zero, because the phase can have 2π-slips, which cause a small average voltage

across the junction. This phase diffusion is a dissipative process and therefore it can be harmful in some applications, for example when a junction is a quantum state detector.
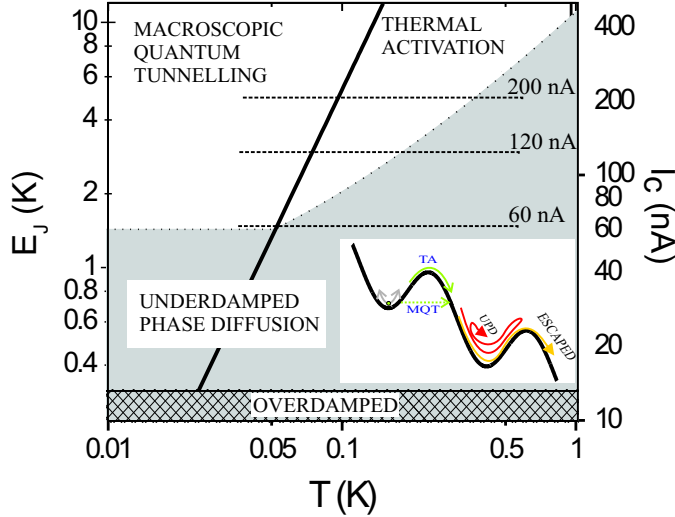

Figure 3.4: The different operation regimes of small Josephson junctions [PI]. The thick black line shows the cross-over temperature T_0 between TA and MQT regimes and the dotted line presents the transition temperature from escape dynamics to underdamped phase diffusion regime. The white area shows the regime, where the conventional escape into a resistive state dominates (with current pulses $\sim 100~\mu$s long and with $\sim 500~\Omega$ shunting impedance). Inset: The tilted cosine potential. The schematic dynamics inside a well (upper well) and *after* leaving the upper well.

We mapped out the behaviour of Josephson junctions with different E_J and at various temperature. The results are summarized by the "phase diagram" of Fig. 3.4 [PI]. The white area describes the region, where switching to the N-state after the escape from one well is certain and thus the switching measurements are possible. In the gray phase diffusion regime the escape does not lead to a free running state, but the phase is moving instead diffusively from one well to another.

The gray phase diffusion area in Fig. 3.4 is divided in the two different regimes: underdamped ($Q > 1$) and overdamped ($Q < 1$) phase diffusion regimes. There is a fundamental difference between these regimes. In the overdamped phase diffusion regime the phase can slide down the potential with almost constant velocity, in contrast to the underdamped phase diffusion, where the phase has, due to an energy argument, to localize in the

succeeding minimum. The thick black line in Fig. 3.4 shows the cross-over temperature T_0 between TA and MQT regimes. The dotted line separating white and gray regimes shows an additional *transition temperature* from simply escape dynamics to underdamped phase diffusion regime.

Underdamped phase diffusion regime

The escape rate is significant in the range of currents where the barrier height is comparable to the thermal energy. For large junctions, $E_J \gg k_\mathrm{B}T$, this is the case, when the bias current is only slightly below the critical current, but for small junctions, this rate can be large even *without* tilting the cosine potential at all. At small critical currents the successive barrier tops are thus close in energy after escaping, because the potential tilting angle is small. If the escape occurs at small enough currents, there is a finite probability that the escape will be followed by immediate relocalization to the next minimum of the potential due to dissipation. In this process, the phase is moving diffusively from one well to another even though the junction can be underdamped and thus hysteretic. Phase diffusion is possible up to a maximum biasing current I_m of [PI]

$$I_m = \frac{4}{\pi Q} I_C, \tag{3.5}$$

where the value of Q corresponds to the damping at plasma frequency ω_p. With currents below I_m, the voltage rise per one escape event is, due to phase relocalization, negligibly small and we are not able to count these events in the switching probability measurements, nor can we measure the average voltage due to these rare phase slip events.

Overdamped phase diffusion

Unshunted hysteretic junctions can be overdamped due to frequency dependent environmental impedance, which usually is of the order of vacuum impedance at high frequencies $[R(\omega_p) \sim Z_0 = 377 \ \Omega]$. Especially this can be the case for samples with small E_J, which usually implies also small ω_p. Small coupling energy ($E_J \sim k_\mathrm{B}T$) yields also large escape rates and further large phase diffusion rates even at low temperatures. If the rate is large enough, the average voltage across the junction is measurable (but still $\ll 2\Delta/e$). This leads to the current-voltage characteristics with a measurable slope also at zero current. Ingold *et al.* have shown that for overdamped junctions this zero-bias resistance can be given by [25]

$$R_0 = \frac{R}{\mathrm{I}_0^2(E_J/k_\mathrm{B}T) - 1}, \tag{3.6}$$

where R is the junction shunting impedance and I_0 is the modified Bessel function.

3.3.2   Energy level quantization

The number of quantized energy levels inside the potential well can be approximated by $N = \sqrt{E_J/2E_C} \, (1 - I/I_c)^{5/8}$, which results in a rapidly falling number of levels with decreasing critical current. For example, for a 1 $(\mu\text{m})^2$Al-AlOx-Al junction with usual oxidation parameters there are of the order of 10 levels at $I = 0$ and about 6 when $I = 0.5I_c$. In this case, the basic continuum approximations do not hold anymore and more adequate models should be used. In publication [PI] we introduced a model, which takes into account the level quantization using the results of Larkin and Ovchinnikov [26, 27]. It also takes into account that the phase particle can relocalize in the succeeding well after tunneling. The scheme of this quantized energy level (QEL) model is presented in Fig. 3.5.
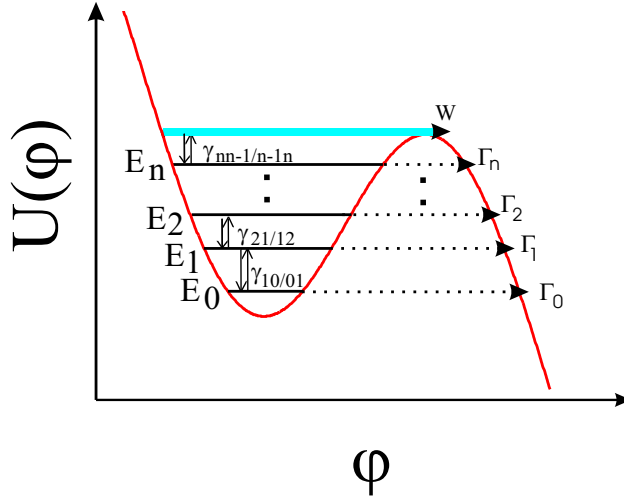

Figure 3.5: The dynamics inside a well. The model of the dynamics considers the transitions (γ_{kj}) between nearest neighbouring levels and the escaping (Γ) out of these levels. The level energies are determined within the nearly harmonic potential.

The total escape probability is calculated using $P_{esc}(\tau) = 1 - \sum_k \rho_k(\tau)$, where $\rho_k(\tau)$ is the probability of finding the particle in level k after the current pulse of length τ. The kinetic equation of the phase particle can be written as $\frac{d\rho_k}{dt} = \sum_j (\gamma_{kj}\rho_j - \gamma_{jk}\rho_k) - \Gamma_k\rho_k$. The model takes into account only

the transitions γ_{kj} between the nearest neighbouring levels and the tunneling out, Γ_k. The positions and escape rates are calculated using the results of Ref. [26].

The possibility for the phase particle to relocalize in the succeeding well after tunneling is taken into account as well. In Publication [PI], we concluded that the level energy E must fulfill the condition

$$\Delta U - E < E_J \left(2\pi I/I_c - 8/Q \right) \tag{3.7}$$

to secure switching into a free running state. If condition of Eq. (3.7) is not fulfilled, the tunneling rate at that energy level is set to zero in the model, $i.e.$, we assume that the thermal distribution in the next well is reached immediately. This assumption holds in most cases, since with the low Q values of our junctions, the phase relaxes in the next well in a time scale, which is far shorter than the typical time interval between phase diffusion events. Note that Eq. (3.7) gives the same threshold as Eq. (3.5) for the special case $\Delta U = E$, but Eq. (3.7) takes into account the fact, that after tunneling the starting point of the phase particle is not at the potential maximum.

3.4   Experimental details and measured samples

The schematic of the experimental setup for switching measurements is presented in Fig. 3.6. Measurements were done in two different $He^3 - He^4$ dilution refrigerators with minimum temperatures around 20-30 mK. The measuring wires were filtered with Thermocoax$^{\circledR}$-lines [28] and π-filters.

Switching probabilities have been measured by applying a set of trapezoidal current pulses, typically 100 μs long, through the sample and by measuring the number of resulting voltage pulses. Current pulses were created by applying voltage pulses either from the PC data aqcuisition card or from an Agilent 33220A function generator through a large (100 kΩ -10 MΩ) resistor. The voltage across the sample was amplified by a large bandwidth pre-amplifier (HMS electronics 568) and recorded by using the same data aqcuisition card. The normal delay time between current pulses was 500 μs, and it was measured to be long enough for cooling the sample after the dissipative switching event.

The I_c of the measured samples were in the range of 100 nA and thus the noise level of the current pulses had to be well below 1 nA. Even a small inductively coupled noise will produce large noise currents, because

the sample resistance is zero in the superconducting state. One possible way to suppress this noise is to use large enough resistors as close to the measured junction as possible. The Joule heating sets the limit for the resistors. We used 500 Ω surface mount resistors. These resistor were found to be essential in measurements of the weak coupling samples.

A ~ 10 kΩ resistor was placed in parallel with the input of the voltage amplifier to speed up the retrapping. This resistor was either at room temperature or at the sample stage. The retrapping time of the junction is limited by the RC time constant of the circuit. Without external resistors, the circuit impedance is given by the large subgap resistance of the junction, yielding long retrapping times. For example with 100 pF capacitance of the measuring lines the usual 10 MΩ subgap resistance gives that the retrapping time is about 1 ms. With the parallel resistor this time is much shorter and, *e.g.*, with 10 kΩ resistor it is around 1 μs. When the junction is in the super-conducting state, the system dynamics are not harmfully affected, as long as the value of the resistor is much larger than the high frequency shunting of the measuring leads ($\sim 100 - 500$ Ω).

Surface mount capacitors (usually 680 pF) were also at the sample stage to form low pass RC-filters close to the junction. The sample was connected
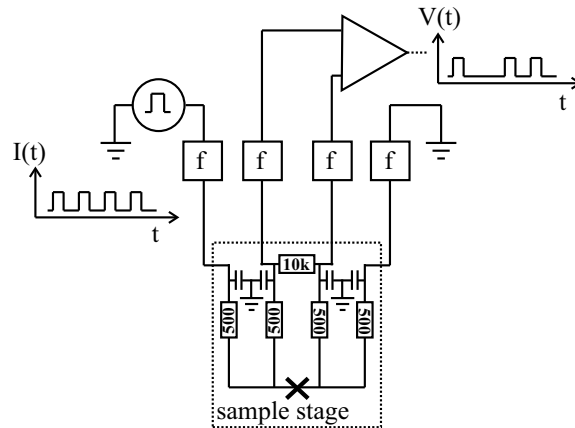

Figure 3.6: The scheme of the escape probability measurements. The parts enclosed by a dashed line are located at the sample stage at millikelvin temperatutes. The "f" represents low pass filters. Every measuring wire consists also of a serial surface mount resistor (usually 500 Ω) close to the sample in order to suppress inductively coupled current noise. In parallel with the voltage amplifier was typically a ~ 10 kΩ resistor either at room temperature or at the millikelvin temperatures to decrease the retrapping time.

to the filters by ultrasonic bonding. The influence of the inductance of the bonding wires ($\sim$1 nH) on junction dynamics was assumed to be negligible.
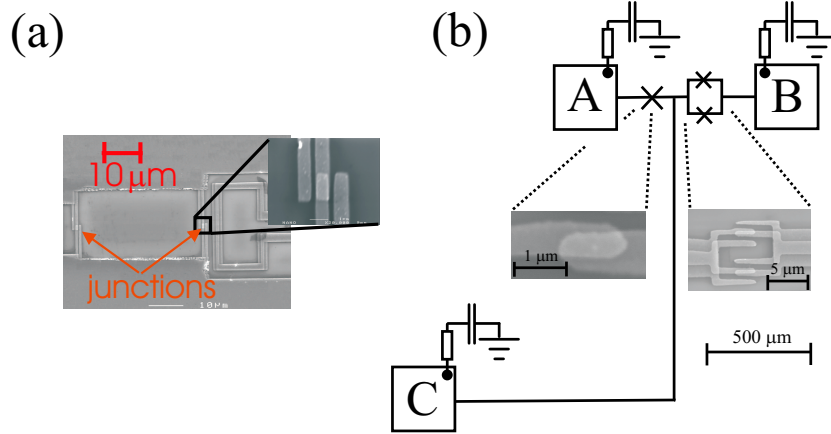
Measured samples

Figure 3.7: (a) The SEM micrograph of the measured dc-SQUID sample (SQ1) and (b) the sample with tunable environment (SQJJ) (b).

Three different samples were measured: a single junction (JJ1), a dc-SQUID (SQ1) and a sample, which consists of both a single junction and of a dc-SQUID (SQJJ). Sample SQJJ was in the weak coupling regime, where E_J is of the order of thermal energy $k_{\mathrm{B}}T$. Samples JJ1 and SQ1 were in the intermediate coupling regime between "standard" strong coupling junctions ($E_J \gg k_{\mathrm{B}}T$) and the junctions with weak coupling. The SEM micrographs of the samples are presented in Fig. 3.7 and the parameters are given in Table 3.1.

Sample SQ1 has a dc-SQUID geometry, which consists of two wide superconducting planes connected with two short superconducting lines with tunnel junctions in the middle, as presented in Fig. 3.7 (a). The purpose of the wide planes was to reduce the loop inductance and the measured inductance 120 pH was indeed small as compared to the calculated Josephson inductance ($L_J = \Phi_0/(2\pi I_c) = 3.2$ nH per junction). Sample JJ1 was a single junction between long inductive biasing lines. The schematic of the sample SQJJ is presented in Fig. 3.7 (b). The sample consists of a single tunnel junction, a dc-SQUID and a long inductive line connected together in the middle. The idea is, that the dc-SQUID is providing a tunable environment for the single junction. The distance between a dc-SQUID and a single junction was approximately 120 μm and the long inductive line was

Table 3.1: The parameters of the measured samples. Both the critical current I_c [Ambegaokar-Baratoff value calculated from the normal state resistance, Eq. (2.4)] and the sample capacitance C_J [calculated based on the junction area and 50 fF/$(\mu\text{m})^2$] are given for the whole tunable circuit in case of dc-SQUID samples.

sample	R_T (kΩ)	I_c (nA)	E_J (K)	C_J (fF)
moderately weak coupling				
SQ1	1.3	199	4.6	100
JJ1	0.41	630	14.5	130
weak coupling				
SQJJ				
single junction	11.6	23.4	0.53	30
dc-SQUID	3.8	74.5	1.7	50

connected in between for separate biasing. The length of the line was around 3 mm leading to an inductance of $\sim l\mu_0 \approx 3$ nH.

Figure 3.8 presents the parameters of the measured Josephson junctions **1.-4.** and of the measured Josephson junctions found in the literature. Junctions far in the $E_C \gg E_J$ regime have been excluded because they obey different physics from what we are interested in here. The observations on the samples **5.-8.** present intensive phase diffusion, in contrast to the samples in the upper left corner, which show simple escape dynamics from the metastable well. The samples studied here fall in the regime, which has not been properly studied until now: the coupling energy E_J is in the order of, but still larger than thermal energy, while the charging energy $E_C \ll k_{\text{B}}T$. In this parameter regime both the simple escape from a single metastable state, and phase diffusion coexist [PI, PII]. Dashed lines in Fig. 3.8 give the approximative number of quantized energy levels inside the well. Weak coupling yields a small number of quantized levels, and thus the continuum approximations are not necessarily valid with low I_c samples. In this case, the level quantization must be taken into account when calculating the dynamics of the system properly [PI].

3.5   Cumulative histograms

Figure 3.9 presents the measured cumulative switching histograms (open circles) of sample SQ1 at fluxes 0, 0.28 Φ_0 and 0.41 Φ_0 at different temperatures. If we assume that the two junctions of the dc-SQUID are identical, we can
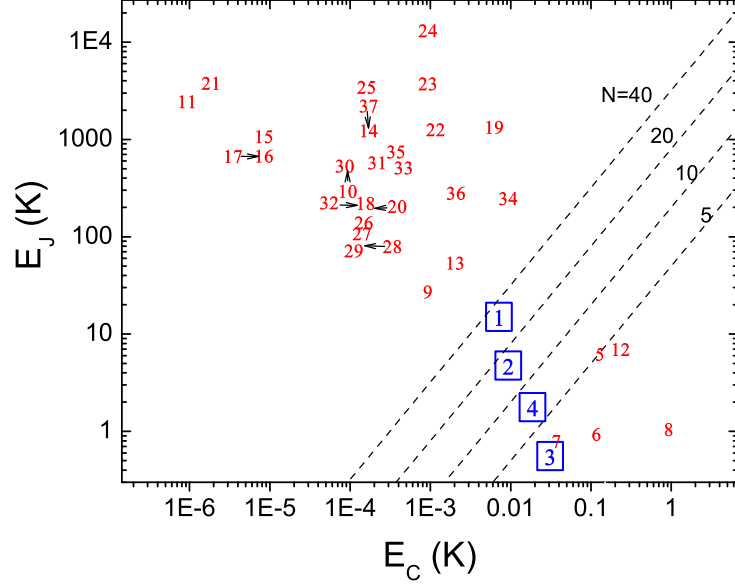
Figure 3.8:   The Josephson junctions measured in this work **1.-4.** and some representative samples from literature on the (E_C, E_J)-plane. Here only samples, which are measured directly, are presented and thus, *e.g.*, flux squbit samples are excluded. Few samples are moved for clarity and black arrows are indicating the correct positions. Dashed lines give the approximative number of quantized energy levels inside the well.

List of samples:
1. SQ1, **2.** JJ1,
3. the single JJ and **4.** the *dc*-SQUID of the sample SQJJ,
5. J. Sjöstrand *et al.* [17], **6.** P. Joyez *et al.* [29],
7. J. Claudon *et al.* [30], **8.** A. Steinbach *et al.* [31],
9. A. Cottet *et al.* [32], **10. 11.** J.M. Martinis *et al.* [33],
12. H. Tanaka *et al.* [34], **13.** F. Balestro *et al.* [9],
14. P. Silvestrini *et al.* [35], **15. 16. 17.** V. Lefevre-Seguin *et al.*, [36]
18. J. Clarke *et al.* [37], **19.** S. Washborn *et al.* [38],
20. M. Devoret *et al.* [39], **21.** P. Silvestrini *et al.* [40],
22. 23. 24 . M. Castellano *et al.* [41], **25.** Y. Yu *et al.* [42],
26. 27. 28. 29. 30. M. Devoret *et al.* [43], **31.** A.N. Cleland *et al.* [44],
32. J.M. Martinis *et al.* [45], **33.** K. Segall *et al.* [46],
34. D.S. Crankshaw *et al.* [47], **35.** B. Ruggiero *et al.* [48],
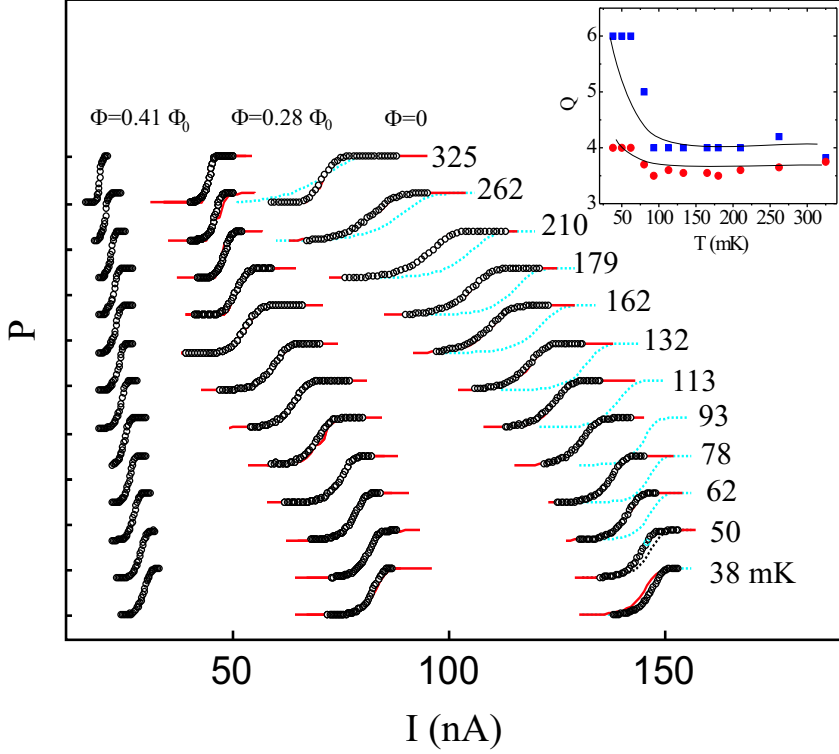**36.** C. Cosmelli *et al.* [49], **37.** B.Ruggiero *et al.*, [50]

Figure 3.9:   Cumulative histograms of a *dc*-SQUID SQ1 at different temperatures. The rightmost curves are measured at zero field and in the left and in the middle we present histograms measured at $0.41\Phi_0$, and $0.28\Phi_0$ respectively. The curves are shifted for clarity and the vertical spacing between ticks corresponds to escape probability of unity. Solid lines are from simulations based on Larkin and Ovchinnikov model [26,27] described in the text. The dotted lines show the results of the basic model where MQT and TA rates are added together. Inset: The squares and circles are the fitted quality factors Q at different temperatures at zero flux and at $\Phi = 0.28\Phi_0$, respectively. The lines are to guide the eye. The number of repetitions at each current was 10^4 and the length of the current pulses was 200 μs.

infer based on Eq. (2.7) that the corresponding critical currents are 200 nA, 128 nA and 55 nA, respectively. Figures 3.10 (a) and (b) show measured histogram positions $I_{50\%}$ [$P(I_{50\%}) \equiv 0.5$] and widths ΔI ($\equiv I_{90\%} - I_{10\%}$) of samples SQ1 and JJ1. The position is normalized to the corresponding

critical current.

The results of the basic TA and MQT model simulations are presented in Fig. 3.10. At low T, all the measured data are consistent with the MQT results. With increasing temperature, the parameters are constant up to the estimated cross-over temperature T_0. Above this, the width of the switching histogram is increasing and the position is moving down, as the TA model predicts. The qualitative agreement is satisfactory for most of the results up to a temperature, which we denote T_D (black arrows in Fig. 3.10). At T_D, ΔI starts to decrease abruptly and the position of the histogram saturates. The phase diagram of Fig. 3.4 presents the critical current of SQ1 at fluxes 0, $\pm 0.28\Phi_0$ and $\pm 0.41\Phi_0$ by horizontal dashed lines. The estimated cross-over temperatures from thermal escape into underdamped phase diffusion regime based on the intersections of the dashed lines and the boundary of the phase diffusion regime in Fig. 3.4 are very close to the experimentally determined temperatures T_D. Hence, the transition into underdamped phase diffusion regime causes the re-entrant steepness of the histograms. The studied samples thus exhibit transition from the MQT regime to the underdamped phase diffusion regime through the TA regime.

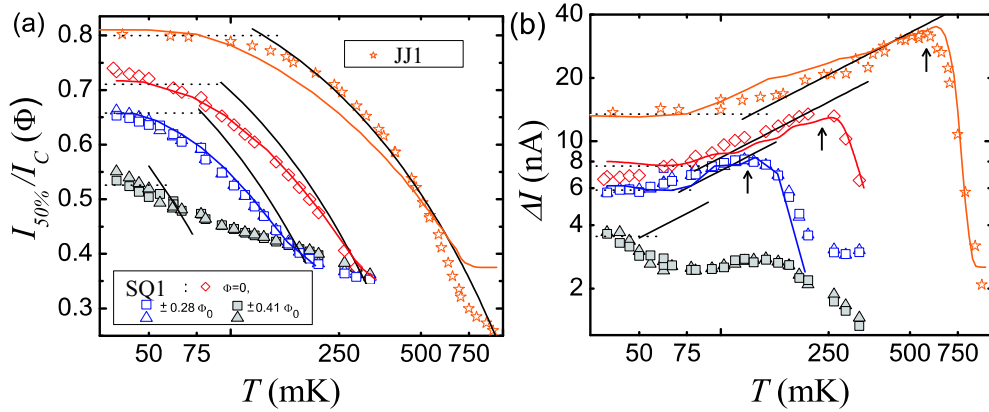Figure 3.9 presents results of the quantized energy level model (QEL)

Figure 3.10: (a) The positions ($I_{50\%}$) and (b) the widths (ΔI) of the histograms of samples SQ1 and JJ1. Black solid and dotted lines are calculated results (with known junction parameters) of TA and MQT model, respectively, ignoring dissipation. Lighter lines are the parameters of the simulated histograms based on the QEL model discussed in the text. The model assumes escape and possible relocalization events to be rare; thus it is not valid for data at $\Phi = \pm 0.41\Phi_0$, where the rate of phase diffusion events approaches the relaxation rate in the well.

simulations for data at zero and $\pm 0.28\Phi_0$ fluxes (solid lines) and also the results of the basic TA-MQT model at zero flux (dashed lines). Figure 3.10 presents the parameters of the simulated histograms (lighter lines) as well. In comparison with the agreement between experiment and TA-MQT model, the agreement of the QEL model simulations with the experiment is excellent. The position and the width of the measured histograms coincide and, in particular, at T_D the simulated histograms also start to get steeper again. In the QEL simulations, the only fitting parameter is the quality factor Q, and the fitted values (presented in the inset of Fig. 3.9) are in a very reasonable range.
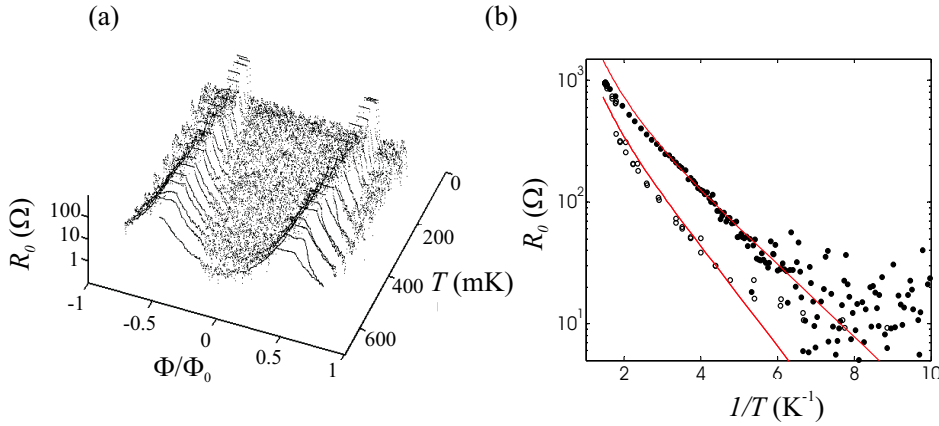
3.6   Zero-bias resistance

Figure 3.11: (a) Zero-bias resistance R_0 of the dc-SQUID of sample SQJJ at different magnetic fields and temperatures. The saturation to 250 Ω, close to half of a flux quantum, is due to the saturation of the lock-in amplifier. (b) Filled (open) circles are the R_0 values of the dc-SQUID (the single junction) of sample SQJJ at $\Phi = 0.42\ \Phi_0$ at different temperatures. Lines are the results of the model for overdamped junctions [Eq. (3.6)] assuming the same fitted value of 270 Ω for shunting resistor in both cases. E_J of the dc-SQUID was estimated based on the working point, $\Phi = 0.42\ \Phi_0$, the normal state resistance, $R_T = 3.8$ kΩ, and assuming a symmetric structure.

Both the single junction and the dc-SQUID of the sample SQJJ are in the overdamped regime. The coupling energy is so small that the phase diffusion rate yields a measurable average voltage across the junction. The zero-bias resistance R_0 was measured at different temperatures by using lock-in technique. The results are shown in Figs. 3.11 (a) and (b). The dc-SQUID

was measured at different magnetic fields. The measurement noise level sets the minimum measurable resistance to somewhere around 10 Ω (the flat region): the amplitude of the measurement *ac* current had to be set to a value which is much smaller than the switching current.

Figure 3.11 shows the results of Eq. (3.6) with a fitted value of 270 Ω for shunting resistance R. The theory closely follows the measurement over two decades in resistance. The zero-bias resistance of the *dc*-SQUID is increasing strongly with decreasing critical current as Eq. (3.6) predicts, see Fig. 3.11 (a). With critical currents of the order of 10 nA, R_0 is larger than 10 Ω even at the lowest temperatures.

3.7   Tunable environment

Zero-bias resistance measurements, described in the previous Section, illustrate that the single junction of sample SQJJ has intensive phase diffusion even at the lowest temperatures. Switching from the phase diffusion branch to the high voltage state is a complicated process and there do not exist in literature similar simple analytical expressions to describe it, unlike, *e.g.*, in the case of the basic thermal activation. Yet, also this thermally activated process is strongly environment dependent. We verified this by Monte Carlo simulations based on Refs. [19, 20]. In the sample SQJJ, the environment of the single junction presented by the *dc*-SQUID is strongly inductive. The Josephson inductance of the *dc*-SQUID at zero field is of the same order of magnitude ($L_J \approx 4.5$ nH) as the inductance of the long line, but it is increasing strongly with increasing magnetic field. The aim of the experiment was to measure how changing the Josephson inductance of the *dc*-SQUID is affecting the switching dynamics of the single junction.
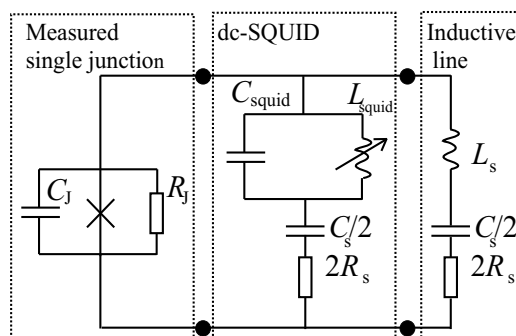

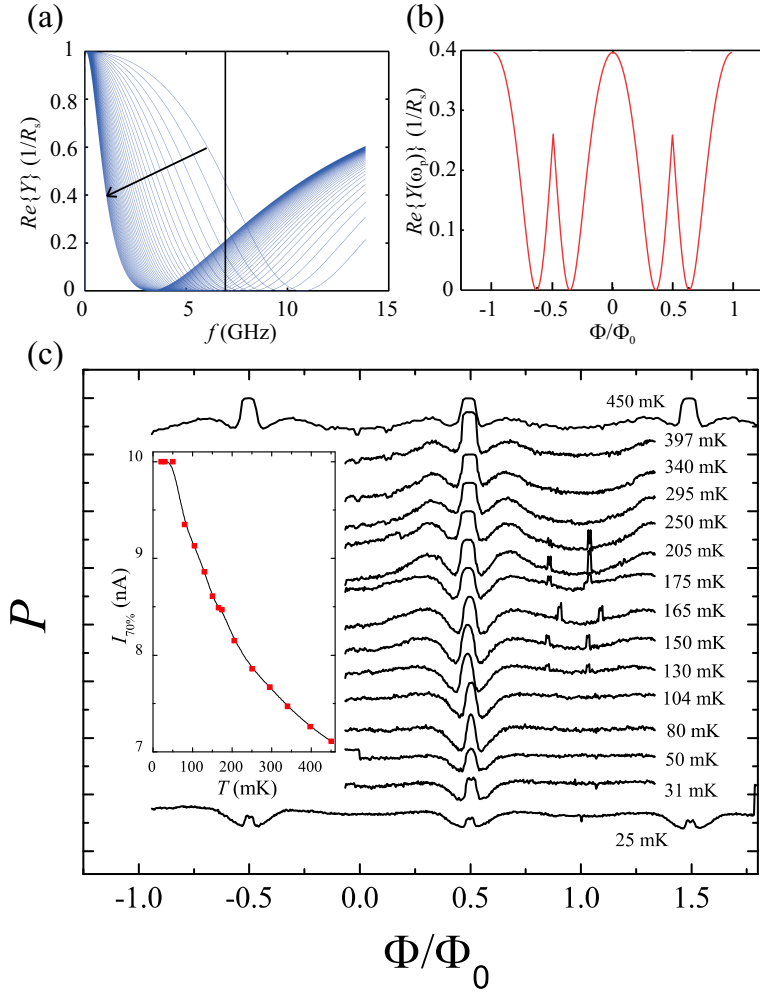Figure 3.12:   Circuit model of sample SQJJ.

Figure 3.13: (a) The real part of the admittance $Re\{Y\}$ of the parallel combination of the dc-SQUID and of the inductive line as a function of frequency at different fluxes between 0 and Φ_0. The vertical line corresponds to the plasma frequency of the single junction at zero bias current. The arrow indicates the direction of increasing Josephson inductance. In calculations we used the value 3 nH for the inductance of the long line and the parameters of the dc-SQUID are given in Table 3.1. (b) $Re\{Y\}$ as a function of flux at the plasma frequency of the single junction. (c) Measured switching probability of the *single* junction of sample SQJJ at constant current bias as a function of applied magnetic flux at several temperatures between 25 mK and 450 mK. Curves are shifted for clarity and the vertical spacing between ticks corresponds to escape probability of unity. Inset: The current, which corresponds to 70 % escape probability at various temperatures, as measured with the single junction of sample SQJJ.

We studied the switching probability of a *single* junction as a function of flux through the dc-SQUID. In the measurement bias current was fed through the single junction line [A in Fig. 3.7 (b)] to the long inductive line (C) and the voltage was measured between these electrodes. At each temperature, the amplitude of the current pulse, which corresponds approximately to 70 % switching probability at zero flux, was measured first. Next, the switching probability of the single junction was measured as a function of flux at this fixed current amplitude. Results are presented in Fig. 3.13 (c). The inset of Fig. 3.13 (c) shows the $I_{70\%}$ -value at zero flux at each measuring temperature.

There is no quantitative model for the flux dependence of the escape rate, but it is obvious that the dc-SQUID decouples the external noise at a certain value of flux. In [PII] we approximate the sample by a model circuit presented in Fig. 3.12. In this model the dc-SQUID is approximated by a parallel combination of a Josephson inductance and junction capacitance [51]. Figure 3.13 (a) presents the calculated real part of the admittance of the inductive line and of the dc-SQUID at different values of flux, which form the environment of the single junction. In calculations we used the value 3 nH for the inductance of the long line and the parameters of the dc-SQUID are given in Table 3.1. At $\Phi = 0$ the plasma frequency of the dc-SQUID is larger than that of single junction due to different thickness of the oxide barriers. With increasing flux, the plasma frequency of the dc-SQUID reduces. Around $\Phi = 0.3\Phi_0$ it coincides with the plasma frequency of the single junction. In Fig. 3.13 (b) $Re\{Y\}$ is presented as a function of flux at the plasma frequency of the single junction. By comparing this with the results presented in Fig. 3.13 (c), we can see that the switching probability follows the general behaviour of the admittance at the plasma frequency. Under this assumption, we can further deduce that dissipation in the zero voltage state takes mainly place at plasma frequency. Further, the energy is dissipated predominantly far away from the junction and the quasiparticle resistance is not playing an important role.

3.8   An example of current detection: shot noise measurements

This Section gives an example of how a hysteretic Josephson junction can detect current or its fluctuations: a Josephson junction in MQT regime is used to measure high frequency current fluctuations generated by a mesoscopic scatterer. The measurement configuration with an electron micrograph of a dc-SQUID detector is shown in Fig. 3.14 (a) and Fig. 3.14 (b) presents
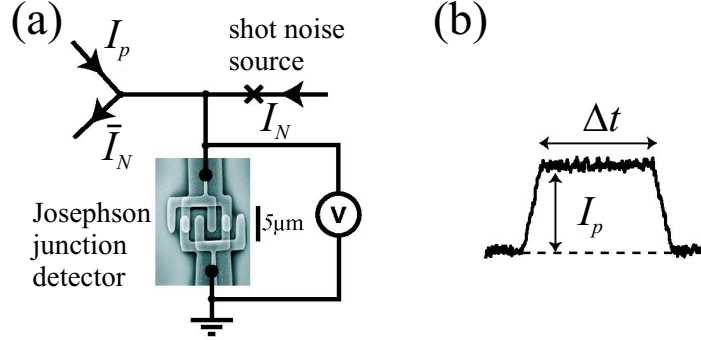
Figure 3.14: (a) Configuration in the shot noise measurements. A *dc*-SQUID in MQT regime measures the current fluctuations due to the shot noise of the scattering junction in the right arm. (b) Sketch of current pulses I_P, with superimposed noise of I_N.

sketch of current pulses. In a typical experiment two currents, I_N and I_P, are injected into the circuit through large resistances (> 1 MΩ) at room temperature. Current I_N is applied constantly and it runs through another tunnel junction at a distance of 120 μm from the detector. This junction plays the role of a shot noise source in the circuit. The *dc*-component of this current, $\bar{I}_N$, returns through a long (3 mm) and narrow (width 2 μm) superconducting line such that no *dc* current due to I_N passes through the detector. Thus, only the fluctuations of I_N are admitted through the detector. In Publication [PIII] we present a model, in which the noisy current excites the phase particle in a metastable, nearly parabolic well out from the ground state, and subsequently the particle escapes from the well. This occurs via thermal activation at an equivalent temperature of the phase particle which is determined by the competition between shot noise excitation, and relaxation due to the dissipative environment. According to this model the effect of these fluctuations can be described by the equivalent temperature

$$k_{\mathrm{B}}T^* \simeq \frac{\hbar\omega_{\mathrm{p}}}{2\operatorname{arcoth}(1 + QFe\bar{I}_N/\hbar\omega_{\mathrm{p}}^2 C)} \tag{3.8}$$

of the phase particle of the detecting Josephson junction. Here F is the "Fano" factor of the noise source and the circuit surrounding the JJ, at the frequency corresponding to level separation. Here it is determined experimentally as a fit parameter.

Following the standard results of the decay from a cubic metastable well, we can infer that thermal activation is the dominant escape mechanism provided $T^* > T_0 \equiv \hbar\omega_{\mathrm{p}}/2\pi k_{\mathrm{B}}$. With this procedure it is then

Table 3.2: Parameters of the two samples in shot noise measurements.

sample	I_C detector	C detector	I_C scatterer	C scatterer
shot-A	3.9 μA	230 fF	600 nA	40 fF
shot-B	1.5 μA	230 fF	15 nA (1)	10 fF (1)
			90 nA (2)	40 fF (2)

straightforward to obtain the switching probability of the threshold detector, in the limit of many levels in the well, as $P(\bar{I}_P) = 1 - \exp(-\Gamma\tau)$. Here $\Gamma = \frac{\omega_p}{2\pi}\exp(-\Delta U/k_B T^*)$ is the standard TA escape rate and τ is the length of the current pulse.

This Section reports on data of two samples, shot-A and shot-B. Sample shot-A had a dc-SQUID detector and one scattering junction as in the scheme of Fig. 3.14. Sample shot-B had a single JJ as a detector, and it had two scattering junctions located symmetrically with respect to the detector (at a distance of 120 μm), and with respect to *two* long injection lines. In this sample the two scattering junctions were made intentionally very different to check the invariance of the results with respect to junction properties. The parameters of the two samples are listed in Table 3.2.

Data in Fig. 3.15 (a) show results of a control experiment on sample shot-B at the base temperature $T \simeq 30$ mK, where the trapezoidal pulse current I was injected through (i) one of the long injection lines, (ii) through scatterer 1, and (iii) through scatterer 2. The histogram of case (i) lies at higher currents than those of (ii) and (iii), which in turn overlap practically with each other. This demonstrates that shot noise tends to push the threshold towards lower values of current, as predicted, *e.g.*, by TA-model with Eq. (3.8). Furthermore these data demonstrate that the noise is predominantly, and equally in (ii) and (iii), generated by the scattering tunnel junctions. The calculated lines run through the corresponding experimental histograms assuming MQT without any noise in (i) and TA with T^* evaluated from Eq. (3.8) with $QF = 5$ in (ii) and (iii). The latter value is realistic in terms of the expected $Q \simeq 10$ [PI] and $F \leq 1$.

Figure 3.15 (b) shows data on sample shot-B at $T = 40$ mK. The threshold current $I_{50\%}$, has been plotted as a function of $\bar{I}_N$ through the scatterer 2. The data, shown by solid symbols, follow the prediction of the model presented above, again with $QF = 5$. The initial plateau in the experimental data below $I_N \simeq 100$ nA arises because the scattering junction is not in the linear
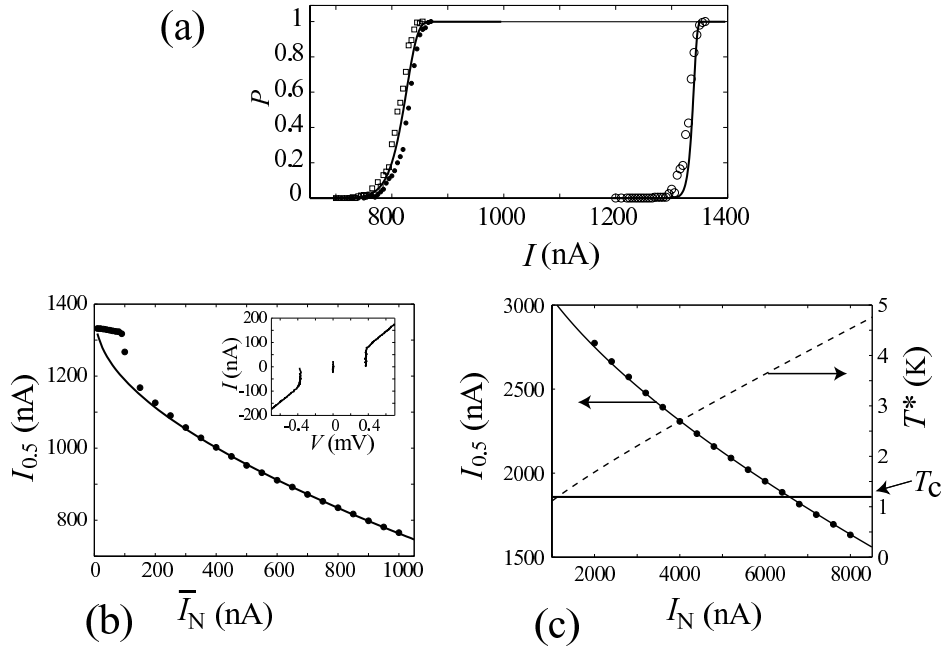
(a)

(b) $\overline{I}_{\mathrm{N}}$ (nA)

(c) I_{N} (nA)

Figure 3.15: Histogram positions under shot noise injection. (a) Escape histograms of sample shot-B when 800 μs long current pulses have been injected through the long injection line (open circles), and through the two noise sources (1 - squares, 2 - filled circles), respectively. The lines are the corresponding theoretical results. (b) Experimental results (circles) on the switching threshold current $I_{0.5}$ against the average current $\overline{I}_{\mathrm{N}}$ through the scatterer 2 in sample shot-B. Pulse length was $\Delta t = 800$ μs. The solid line is again the result of the used theoretical model. The inset shows the IV curve of the noise source. (c) Similar data as in (b) but for sample shot-A. The rising curve shows the corresponding equivalent temperature T^*, which ranges from 2 to 5 K in this measurement.
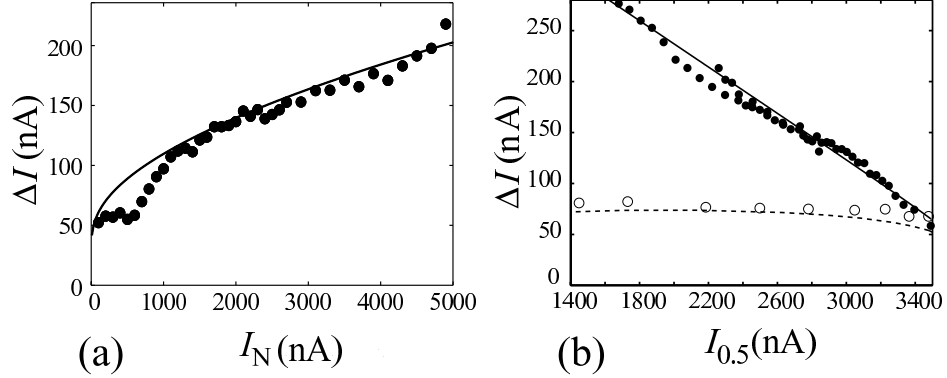
Figure 3.16: The width of the histograms when shot noise and thermal noise are applied. (a) ΔI against the average current $\bar{I}_N$ through the scatterer. The dots are the experimental results and the solid line is the result of the theoretical model. (b) ΔI vs. $I_{50\%}$ under two different experimental conditions. The filled circles are data with elevated shot noise temperature T^*, whereas the open circles are with variable bath temperature T. The solid line is the result of thermal activation model with constant energy gap, and the dashed line takes into account the suppression of the BCS gap [5] in the measurement with increased T.

quasiparticle tunneling regime here which might yield experimental artifacts. The inset of Fig. 3.15 (b) shows the IV curve of this junction. Fig. 3.15 (c) presents, in addition to similar data as in (b), the equivalent temperature T^* in the measurement of sample shot-A when current $\bar{I}_N$ is varied between 2 μA and 8 μA.

Figure 3.16 (a) shows the width of the switching threshold, ΔI, of sample shot-A. In Fig. 3.16 (b) data on switching of sample shot-A have been plotted in two different experimental conditions, in each case as ΔI vs. $I_{50\%}$. The open circles are data where the bath (lattice) temperature has been varied by heating the sample stage to several temperatures T in the range 0.03 - 1 K. The full circles are data taken at the base temperature of the cryostat ($T \simeq 30$ mK), but by varying the equivalent temperature T^* injecting different levels of $\bar{I}_N$. The line closely following the latter data is that originating from the thermal activation model. At the first sight it is surprising that the truly thermal data (open circles) fall far below this line and the other set of data. This is, however, accounted for by the fact that when increasing the bath temperature close to T_C of aluminium (~ 1.2 K), the BCS energy gap is progressively diminishing, thus leading to decrease of the critical current. The dashed line following closely this data set is obtained by using the very same thermal activation model, but by taking into account suppression of

the BCS gap due to temperature T [5]. This figure thus demonstrates that the thermal activation model is in good agreement with the shot noise data, and that it is indeed possible, by promoting shot noise, to study Josephson dynamics at temperatures above T_C without suppressing superconductivity.

The model is in excellent agreement with the experimental results, and we were able to investigate Josephson phase dynamics up to equivalent temperatures which are about four times higher than the critical temperature of the superconductor. This is the temperature responsible for phase dynamics: the electrons and lattice of the superconductor are only weakly coupled to this subsystem, and the former two remain essentially at their base temperature.

3.9   Summary

The current sensitivity of a Josephson junction ammeter is increasing with decreasing I_c and this work studies how the dynamics of the JJ is changing towards small I_c. The measurements confirm that dissipation plays a more important role in the phase dynamics of Josephson junctions when the critical current decreases. The parameters of the measured samples were in the intermediate range, where the simple escape from a single metastable state, and phase diffusion coexist. For relatively large E_J, the usual transition between macroscopic quantum tunneling and thermally activated (TA) behavior was observed by varying the temperature. Above this cross over temperature, the observations introduced an additional transition from escape dynamics to underdamped phase diffusion, where the threshold for switching into the finite voltage state becomes extremely sharp. The sensitivity of Josephson junction threshold detection is determined by the steepness of the cumulative histograms. However, in the underdamped phase diffusion regime the re-entrant steepness is due to missed escape events and relocalization, and it might be harmful in some detector applications, where dissipation is to be avoided.

Observations also show that with small I_c one has to take quantized energy levels into account for getting satisfactory agreement between theory and measurements. The agreement between the measurements and the model presented here was excellent and, in particular, it explains the re-entrant steepness of the cumulative histograms quantitatively.

The studies with tunable environment show that switching into high voltage state depends strongly on the environment. These measurements also show that the inductive leads can provide a way to further decrease the critical current without losing the beneficial properties of detector.

The last Section of this Chapter gives an example where a Josephson

junction was used in measurements of shot noise. The experimental and theoretical results are in excellent agreement with each other. We were able to study Josephson dynamics of a JJ up to temperatures $T^* \simeq 5$ K, about four times above the critical temperature T_C of aluminium. Based on the invariance of the obtained results, especially in terms of results on different scatterers on the same sample, see Fig. 3.15 (a), it is plausible that this kind of a detector could be made into an absolute on-chip detector of Fano-factors [52], and noise in general, by careful tailoring of the circuit surrounding the JJ and by measuring Q independently, *e.g.*, in similar way as in [PI].

Chapter 4

Cooper pair pumping

A charge pump is a device which can periodically transfer a discrete amount of charge Q through an electrical circuit. Repetition of the pumping sequence at frequency f would then yield a current $I = fQ$. An accurate charge pump would naturally introduce a perfect current source, but it has also been suggested to be used for closing a so-called *quantum metrological triangle*. This connects basic electrical quantities together fundamentally via natural constants e and h [53]. The *ac* Josephson relation, Eq. 2.5, connects voltage to frequency. On the other hand quantum-Hall effect connects current to voltage via *resistance quantum*, which is $R_q = h/(2e)^2$ for Cooper pairs . Hence, the device, which connects current and frequency, would close the triangle and relate the quantities exactly. One possible way to obtain frequency locked current is indeed to use charge pumps.

There exists many demonstrated charge pump realizations, *e.g.*, a Surface-Acoustic-Wave (SAW) pump [54] and electron pumps based on arrays of small tunnel junctions. The seven junction single electron pump has been demonstrated to be able to transfer charge with an error rate as low as 10^{-8}, but in this case the maximum current is only of the order of 1-3 pA [55]. This current is too small for metrological applications. The SAW-pumps are able to produce larger currents, but in this case the drawbacks are lower accuracy, $\sim 10^{-4}$ until now, and the fixed pumping frequency.

In a single electron pump synchronization is lost when pumping frequency approaches the inverse RC time constant (R is the resistance and C is the capacitance of the tunnel junction). In adiabatic Cooper pair pumping one is transferring electron pairs elastically across the system, and the accurate operation frequency could probably be pushed higher. In this case adiabacity requirement is limiting the operation frequency to values below $E_J^2/(E_c\hbar)$ [56, 57], which is usually of the order of a few 100 MHz. Above this the probability of the Landau-Zener level crossing, *i.e.*, the transition to excited

state, starts to be significant.

The main source of errors in Cooper pair pumping is the cotunneling due to coherent nature of Cooper pair tunneling [58, 59, 60]. Especially in short arrays cotunneling is decreasing accuracy significantly, and thus by increasing the length of an array one would obtain better accuracy, but this would decrease the operation frequency [58]. However, cotunneling can be suppressed in other ways as well, *e.g.*, by embedding the pump in a dissipative environment [61] or by controlling E_J in addition to the gate charge [62].

The beginning of this Chapter concentrates on studies on transport properties and performance limitations of a double island, gate charge controlled Cooper pair pump [PIV], whereas second half deals with a experimental demonstration of the operation of a novel flux assisted single island pump [PV].

4.1   Experimental details

The experimental setup in the two Cooper pair pumping experiments is shown in Fig. 4.1. All measurements were done by using a S.H.E. Corporation DRI-420 $He^3 - He^4$ dilution refrigerator, whose minimum temperature is around 20 mK.

For *low frequency* signals the refrigerator had 14 highly filtered lines [Fig. 4.1 (a)]. These lines include a 3-stage low pass filtering at different temperatures. At room temperature we used commercial low pass π-filters (Tusonix 4101, 55 dB at 100 MHz). Between 600 mK plate and 60 mK plate, each line had 1.5 m of Thermocoax$^{\circledR}$, which also form next filter stage (-200 dB at 20 GHz) [28]. The last filtering stage was at the sample stage at the base temperature. These filters were commercial stress gauges (KYOWA KFG-2-350-D1-23) squeezed between two ground plates forming continuous RC strip line filters [63]. There were four lines for *high frequency* signals as well. Figure 4.1 (a) also presents a scheme of these lines. As a whole the high frequency lines have -33 dB attenuation at low temperature: -20 dB at 4 K, -10 dB at 600 mK and -3 dB at the sample stage temperature (Inmet fixed attenuators). At the sample stage, the high frequency lines were connected to a coplanar transmission line. The sample was directly ultrasonicly bonded to this by using Al bonding wire.

All *dc* voltage measurements are done by using HMS electronic 568 low-noise pre-amplifiers and current is measured using DL-instruments DL 1211 amplifier. Both amplifiers were powered by battery sources only. Between a preamplifier and a data acquisition (NI PCI-6036E DAQ) card a home made battery powered analog optoisolation circuit was used to avoid ground loops
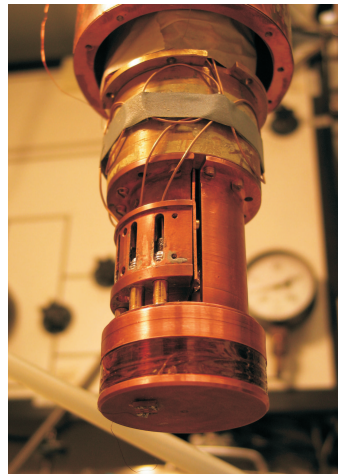
(a)
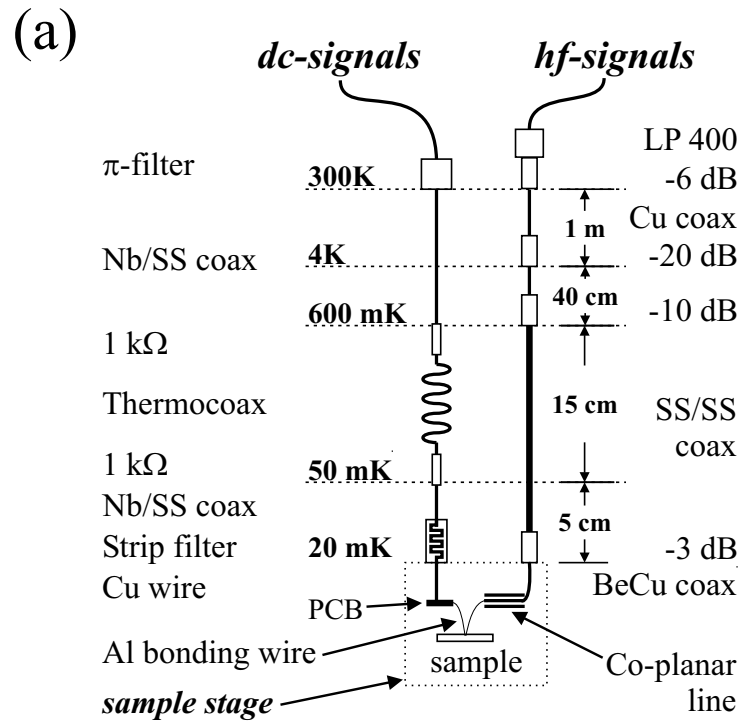
(b)

Figure 4.1: (a) A schematics of measurement wiring of the dilution refrigerator used in Cooper pair pumping experiments. (b) A photograph of the used sample holder. At the bottom of the figure one can see the external coil wound around the cap of the sample stage. Thick wires are BeCu-coaxial cables for high frequency signals.

and digital noise.

4.2   A double island Cooper pair pump

The conventional Cooper pair pump consists of two or more small supercon-
ducting islands in series. We investigated a pump with three junctions and
two islands, which is schematically presented in Fig. 4.2 (a). Each junction
j can be characterized by its coupling energy $E_{J,j}$ and capacitance C_j. The
islands are coupled to the gate electrodes with capacitance $C_{g,i}$ similarly as
in the SET. By presenting the normalized gate charge $q_i = V_{q,i} C_{q,i}/2e$ ($V_{g,i}$
is the gate voltage), and assuming a symmetric island $C_1 = C_2 = C_3 \equiv C_J$,
the system charging energy can be written into a form [PIV]

$$E_{ch} = \frac{4E_c\lambda_g}{\lambda_g^2 - 1}[u_1^2 + u_2^2 + \frac{2}{\lambda_g}u_1 u_2 - \frac{C_J V}{e}(\frac{u_1}{\lambda_g} + u_2)] - 2peV, \qquad (4.1)$$

where $u_i \equiv n_i - q_i$ and n_i is the number of extra Cooper pairs on island i,
$E_c = e^2/2C_J$ is the unit charging energy and $\lambda_g \equiv 2 + C_g/C_J$. The last
term $-2peV$, describes the energy taken from the voltage source at voltage
V when p Cooper pairs have tunnelled through the array.

Equation (4.1) yields a honeycomb like structure on the (q_1, q_2)-plane as
presented in Fig. 4.2 (b) at zero bias. Inside each hexagon the given charge
configuration is stable and it minimizes the system energy (the indices $|lr\rangle$
in the figure indicate the number of extra Cooper pairs on the left and on
the rigth island). At the edges of the hexagons the different charge states
are degenerate. The Josephson coupling energy removes this degeneracy
by introducing coupling between charge states and the new eigenstates are
superpositions of these. Hence by varying gate voltages one can adiabatically
go from one stable hexagon to another.

The principle of Cooper pair pumping with long arrays is presented, *e.g.*,
in Refs. [60,58,59]. Figure 4.3 illustrates a pumping scheme in a double island
pump. Arrows enclosing one triply degenerate node in Fig. 4.3 (a) present
two different pumping paths. The idea is the following: starting from the
origin, the initial condition is $|00\rangle$ (zero extra pairs in the array). By varying
gate voltages slowly from origin to the next hexagon right, the system is adi-
abatically transferred to state $|10\rangle$. In the transition from the right hexagon
to the upper one ($|10\rangle \rightarrow |01\rangle$), the pair is coherently tunneling through the
middle junction and by setting the two gate voltages back to zero the initial
condition $|00\rangle$ can be resumed. Thus the sequence $|00\rangle \rightarrow |10\rangle \rightarrow |01\rangle \rightarrow |00\rangle$
transfers adiabatically charge from left electrode to the right one. The gating
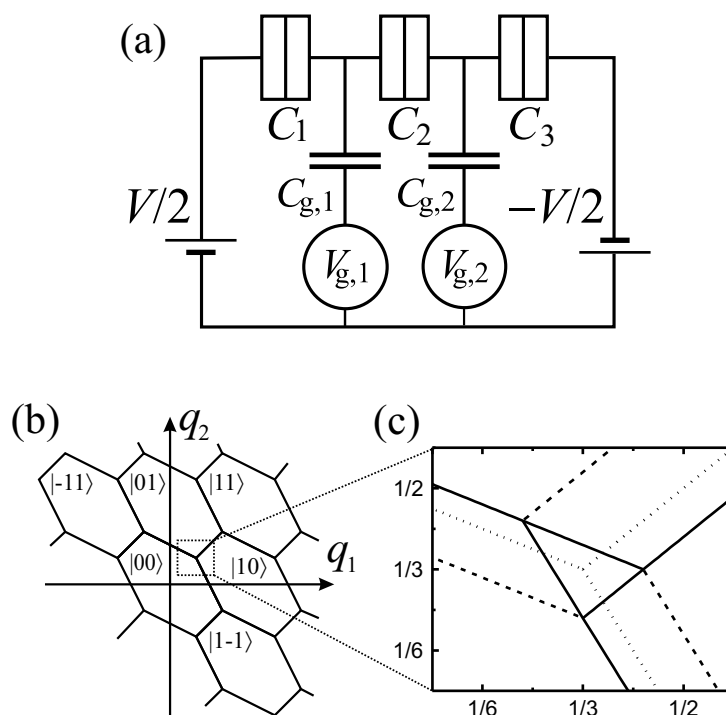sequence needed to produce the triangular path is presented in Fig. 4.3 (b).

Figure 4.2: (a) Double island Cooper pair pump (CPP). (b) The charge states of the Cooper pair pump with the lowest total energy at zero bias on the (q_1, q_2)-plane. Here q_i is the normalized gate charge $q_i = V_{q,i} C_{q,i}/2e$. (c) A close-up of the area near one of the intersection points at bias voltage $C_J V/2e = 0.1$. The solid and the dashed lines show the resonance condition for direct Cooper pair tunneling and for cotunneling, respectively. The dotted line presents the degeneracy lines at zero bias.

Sinusoidal gate pulses with $\pi/2$ phase difference would produce the circular path presented in 4.3 (a) in addition to triangular path.

Figure 4.2 (c) shows the close-up of the area near the triply degenerate node at non-zero bias $C_J V/2e = 0.1$ (the dotted line shows the zero bias condition). The solid lines are presenting the resonance condition for direct Cooper pair tunneling and the dashed lines show the resonance conditions for cotunneling. Here the resonance means that the initial and the final charge states have the same energy. Cotunneling is a second order process, and here it means that the Cooper pair is tunneling through two junctions, $e.g.$, in the transition $|00\rangle \rightarrow |10\rangle$ the Cooper pair tunnels from the right electrode to the island. At zero bias the resonance conditions for direct and cotunneling coincide.

It can also be seen in Fig. 4.2 (c) that with non-zero bias voltage the direct
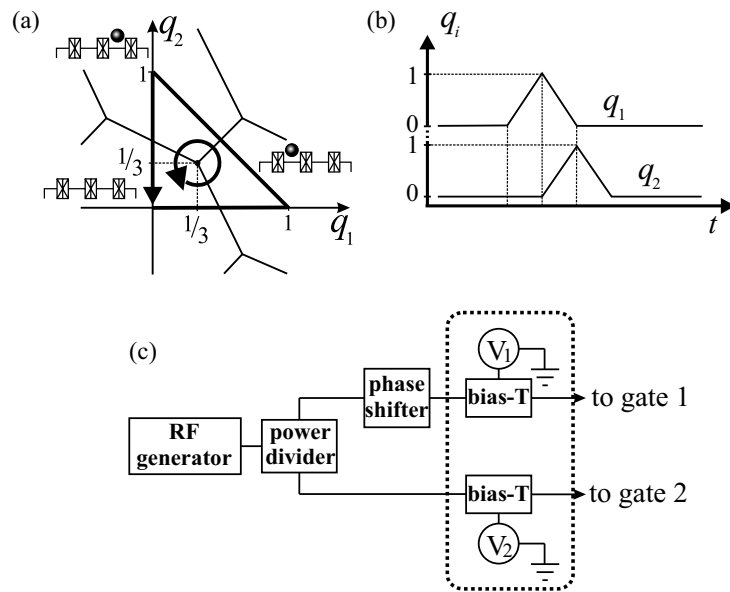
Figure 4.3: (a) Stability diagram of the double island pump close to origin. Arrows enclosing one triple degenerated node are indicating two different pumping paths. (b) The gating sequence needed to produce the triangular path presented in (a). Sinusoidal gate pulses with $\pi/2$ phase difference would produce the circular path presented also in (a). (c) A schematic of the circuit used for producing gating signals. A common high frequency signal generator was used for both gating signals and the needed phase difference was adjusted after power dividing.

tunneling resonance lines do not meet at a point anymore; the degeneracy nodes are split into triangles. Inside the triangle the charge state of the system depends on the path along which the system has entered the particular point on the (q_1, q_2)-plane. The system thus exhibit hysteretic behaviour and this provides the way to use it as a charge *turnstile* [64, 65] in addition to charge pumping. This turnstile experiment is not discussed in this overview part, but a detailed picture can be found in [PIV].

4.2.1   Results

The SEM micrograph of the studied two island Cooper pair pump is presented in Fig. 4.4. The large triangular gray areas in Fig. 4.4 (a) are connected to the gate lines in Fig. 4.4 (b) (the long vertical lines in the interdigital structure). The large ground planes illustrated by black area in Fig. 4.4 (a) and the interdigital gate structure are used for suppressing the cross capacitance between gate lines. The Josephson coupling energy per junction was $E_J/k_B \approx 0.2$ K and the measured charging energy of the islands was $E_C/k_B \approx 1.5$ K. Here we assume that the junctions are identical, and the given E_J is the Ambegaokar-Baratoff value, Eq. 2.4, based on the normal state resistance. The charging energy is determined by measuring the zero-bias conductance at 4.2 K [66].

A schematic picture of gate connections is shown in Fig. 4.3 (c). A common HP8656B signal generator was used for the two gates and the needed phase shift was adjusted after an INMET 6014-2 power divider. The circuit enclosed by the dashed line in Fig. 4.3 (c) presents the custom made electronics for CPP measurements [1]. This device enables one to add the *dc* offset to the pumping signal and to compensate for cross-coupling between the two gate lines.

IV-characteristics and 2D gate modulation

A measured *IV*-characteristic of a double island Cooper pair pump is presented in Fig. 4.5 (a). Figure 4.5 (b) shows a close-up of it near zero bias. Peaks near zero voltage present supercurrent, and they show strong modulation when gate voltage is varied.

To find a proper pumping path, one has to measure the experimental stability diagram, *e.g.*, by mapping the gate dependence of supercurrent $I_s(V_{g,1}, V_{g,2})$. The measured gate voltage modulation of the supercurrent at small bias voltage $V_{bias} \simeq 15\ \mu V$ is presented in Fig. 4.6. A lighter colour

---

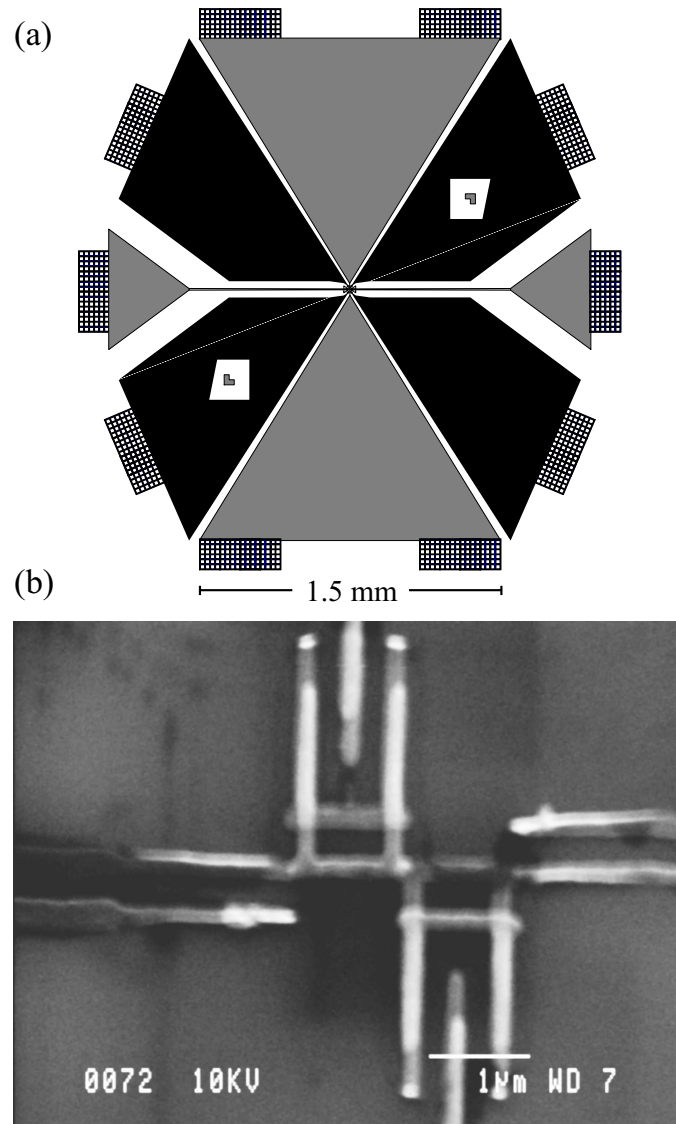[1]Designed and manufactured by Kari Loberg, University of Jyväskylä.

Figure 4.4: (a) Scheme of the large structures of the double island Cooper pair pump and (b) the scanning electron microscope micrograph of the small structures of the sample. The thin horizontal line in (a) and (b) is for sample biasing. The large triangular gray areas in (a) are connected to the gate lines in (b) (the vertical lines in the middle of the fork like structure). The large ground planes presented by black areas in (a) and the interdigital gate structure are used to suppress the cross capacitance between gate lines.
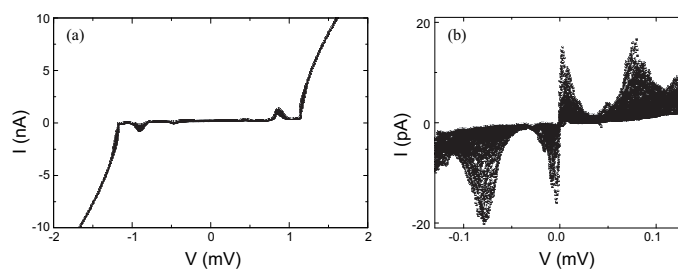
Figure 4.5: (a) An *IV*-characteristic of a double island Cooper pair pump. (b) A close-up of the supercurrent region of (a) plottes at many different gate voltages.
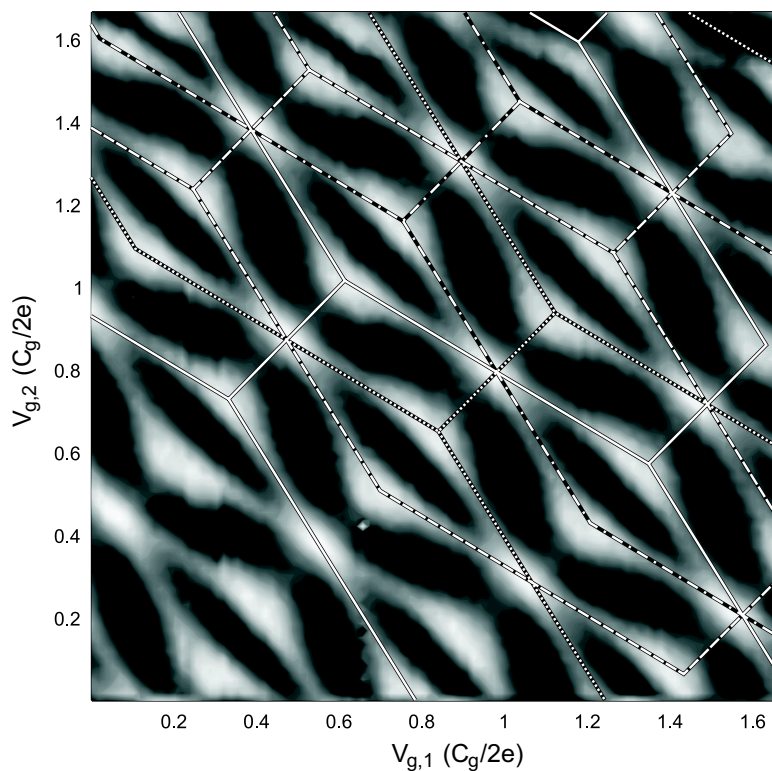

Figure 4.6:   The measured current at different values of the gate voltages in the small bias voltage $V_{bias} \simeq 15 \ \mu V$ regime. Lighter colour corresponds larger current. The measured structure is a composition of four different 2e-periodic structures, each corresponding one possible quasiparticle configuration. Lines drawn in the figure present theoretical degeneracy lines with fitted gate and cross capacitances. Different lines are shifted by 1e corresponding to one extra quasiparticle on one of the islands.
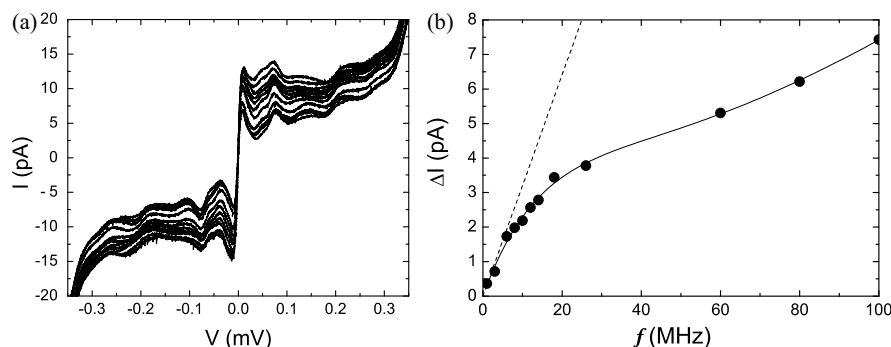
Figure 4.7: (a) IV-characteristics of a double island Cooper pair pump with circular pumping path at various pumping frequencies between 100 kHz and 22 MHz. The absolute value of the current is increasing with increasing frequency. (b) The difference of the current ΔI as a function of pumping frequencies. The data has been taken at the bias voltage $V = 365$ μV.

corresponds to larger current. Since the tunneling probability is greatly enhanced near the resonance condition, the modulation of the supercurrent should produce a similar picture in $(V_{g,1}, V_{g,2})$-plane as what is presented in Fig. 4.2 (b). Yet, we can see that the measured structure differs from the expected one. The structure is $1e$-periodic, which indicates the existence of non-equilibrium quasiparticles. Yet, the structure can not be explained by pure quasiparticle tunneling either, because it would also lead to the simple honeycomb structure with $1e$-periodicity. Instead of one hexagonal honeycomb structure, the measured modulation consists of four of those, each shifted by $1e$ in x- and y-axis directions. This can be explained by assuming that each of these structures corresponds to one of the four different distinguishable quasiparticle configurations $(0,0)$, $(1,0)$, $(0,1)$, or $(1,1)$. Here the indices refer to the number of extra quasiparticles in the first and in the second island. In this "quasiparticle poisoning" picture the charge is mainly carried by Cooper pairs and the effect of the rare quasiparticle tunneling events is to change the offset of the dc gate voltage.

Results of pumping measurements

In a Cooper pair pumping experiment two sinusoidal signals with a $\pi/2$-phase shift were applied to the gates. These signals have dc offsets corresponding to the chosen degeneracy point in the measured honeycomb structure. As a result the signals formed a nominally circular path around a degeneracy point as presented in Fig. 4.3 (a).

Measured IV-characteristics with pumping signals at various pumping frequencies between 100 kHz and 22 MHz are presented in Fig. 4.7 (a). We can see a clear frequency dependence. The pumped current follows, however, always the direction of the bias voltage against the expectations. Furthermore, the IV-characteristics exhibit a strong undesired leakage current. For more detailed analysis this leakage current should be subtracted. This was done by calculating the current difference ΔI between the measured current and that at the lowest 100 kHz pumping frequency. At this frequency the pumped current is negligibly small, but the leakage current is still averaged over the pumping path. One can not use the current which is measured without the pumping signal as a reference, because the leakage current is strongly depending on the gate voltages. Figure 4.7 (b) presents an example of ΔI at different pumping frequencies. The expected $I = 2ef$ dependence is presented by the dashed line, which is close to the measured low frequency dependence. However, with increasing frequency the measured current starts to lack behind probably due to the Landau-Zener level crossing. Yet, the current tends to increase again at the higher frequency, which could not be explained with the simple level crossing model. The solid line in Fig. 4.7 introduces a model, which takes a frequency dependent leakage into account. This model is described in more detail in [PIV].

4.2.2   Discussion

Measured IV-characteristics with pumping signals exhibit a clear frequency dependence, and the measured current is close to the expected value when the pumping frequency is low. The drawback in the measurements on a double island pump was that the direction of the pumped current was set by the bias voltage and not by the relative phase of the gate voltages. The most probable reason for this is extensive cotunneling. Figure 4.2 (c) presents that at non-zero bias voltages the resonant lines for sequential tunneling and cotunneling differ. When the pumping path is against the bias voltage, the cotunneling resonance is reached *first* and the tunneling occurs in the direction of the bias voltage. The IV-characteristic also shows undesired leakage under the pumped current, which would also indicate a large cotunneling rate.

The measured 2D gate modulation map shows a honeycomb structure with 1e-periodicity indicating the existence of non-equilibrium quasiparticles. However, the measured structure could only be explained with the model, where the main charge carriers are Cooper pairs and rare quasiparticle tunneling events are just changing the offset of the gate voltage. The resulting gate modulation structure is a composition of four different 2e-periodic structures. The chosen pumping path is valid only for *one* of the

four distinguishable quasiparticle configurations and with purely stochastic quasiparticle tunneling, the time averaged pumped currents would then be just one fourth of the expected one. Nonetheless, the general trend of the fitted values is that at low frequencies the average number of pairs pumped per cycle is very close to one. This observation indicates that at close to degeneracy the quasiparticle configuration is stable and the quasiparticle tunneling rate is very small.

4.3   A single island flux assisted Cooper pair pump

The flux assisted Cooper pair pump, nicknamed a sluice, consists of a single superconducting island similarly as a SET, but the bare Josephson junctions are replaced by dc-SQUIDs [62]. Figure 4.8 (a) shows a scheme of the sluice. The basic idea of the sluice is that in addition to the gate charge also the Josephson coupling is tuned with the help of small coils near to the dc-SQUID loops. The most remarkable benefit is that the E_J is large only when it is necessary, and only across one junction at a time. Thus the most crucial error sources of the conventional Cooper pair pumping, cotunneling and leakage current, can be avoided at least in principle.

The pumping scheme is presented in Fig. 4.8 (b). In the initial condition $\Phi_0/2$ flux is threading both the dc-SQUIDs and thus both Josephson couplings vanish. The gate charge is initially tuned far from the degeneracy points. Next the gate charge is changed from one charge state to another and at the moment when it is close to a degeneracy value the flux through *one* of the dc-SQUIDs is tuned away from the initial $\Phi_0/2$ value. This introduces coupling between the initial and the final charge states and the system can transit adiabatically between these two. In the transition tunneling takes place through the selected dc-SQUID and the direction of charge transport can hence be chosen. Finally the gate charge is moved back to its initial value, but now the coupling is established across the other dc-SQUID and tunneling thus occurs through this one. Eventually the charge is adiabatically transferred from one electrode to another. It is noteworthy that this charge can also be made a multiple of Cooper pairs instead of just one by increasing the amplitude of the gate variation.

4.3.1   Results

The electron micrographs of a sluice pump are shown in Fig. 4.9. The structure is designed to have large mutual inductance between the dc-SQUID
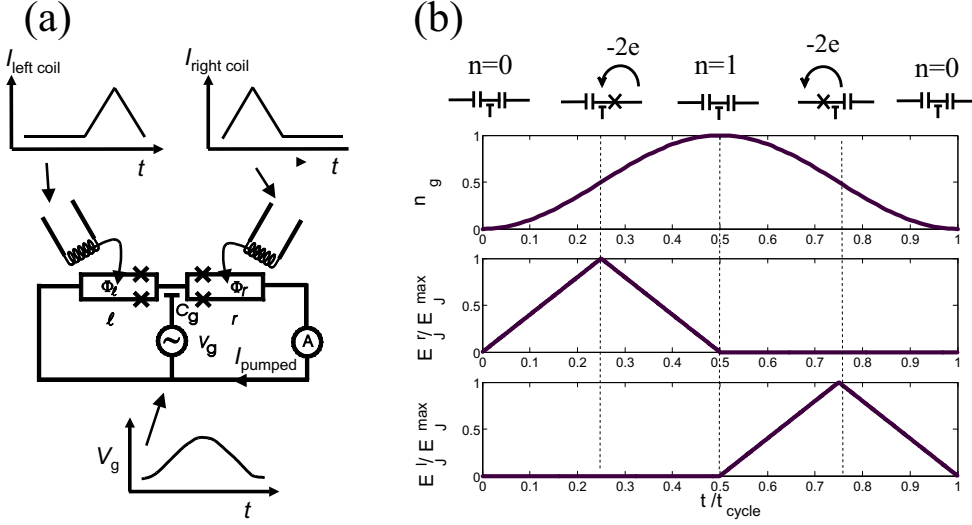
Figure 4.8: (a) The flux assisted Cooper pair pump consists of a single island connected to two dc-SQUIDs. The coupling energy between the island and the electrodes can be tuned by applying current though small coils close to dc-SQUID loops. The gate voltage controls the island charge. (b) Scheme of the parameter sequences to transfer one Cooper pair through the device.

loops and the control coils, yet keeping the undesirable cross-inductances small enough. The needed large mutual inductance also yields a moderately large self inductance of the dc-SQUID. The charging energy should be large enough which sets an upper limit for junction area. Further this means that with usual oxidation parameters the tunnel junction resistance is large, which yields a small coupling energy E_J. Consequently the Josephson inductance is large and $\beta_L \equiv \frac{2\pi L_{loop} I_c}{\Phi_0} \ll 1$, which implies that the dc-SQUIDs can be considered as a tunable Josephson junctions even with moderately large loop inductances. The Josephson coupling energy of the sample was $E_J/k_{\mathrm{B}} \approx 1$ K and the charging energy was $E_c/k_{\mathrm{B}} \approx 1$ K. The given coupling energy is the Ambegaokar-Baratoff value and the charging energy is calculated from the zero bias conductance at 4.2 K similarly as in the case of the double island pump.

The experimental setup is presented in Fig. 4.9 (c). In the pumping experiment the gate charge and both dc-SQUID fluxes were controlled with similar Agilent 33220A arbitrary waveform generators. The three generators were synchronized and the relative phases could be tuned independently.
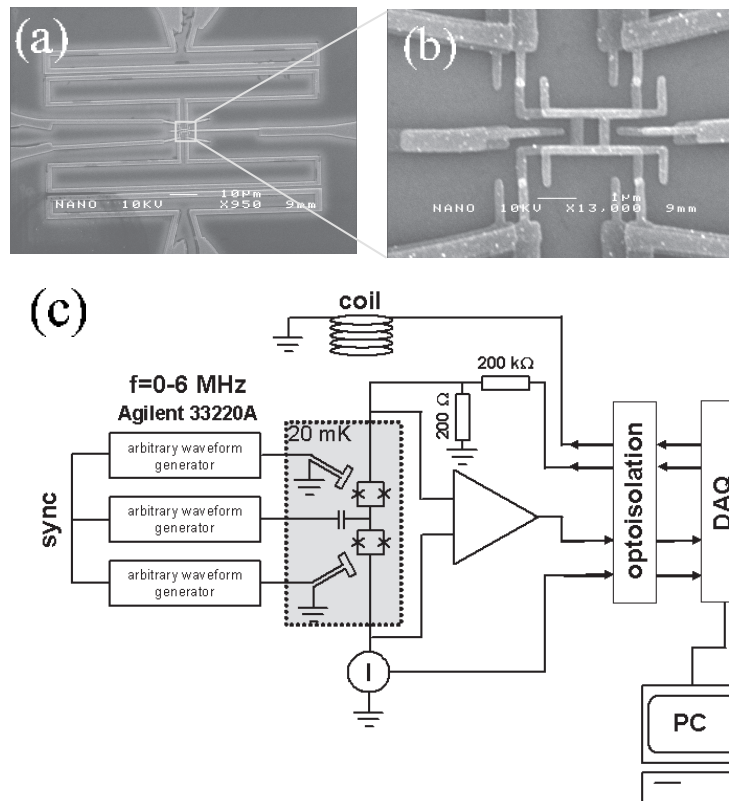
Figure 4.9:   (a) A scanning electron micrograph of a sluice pump sample.
The loops at the bottom and top of the figure are the input coils. (b) The
SEM micrograph of the island. The line in the left of the figure presents
the gate capacitor and the line in the right is just for making the structure
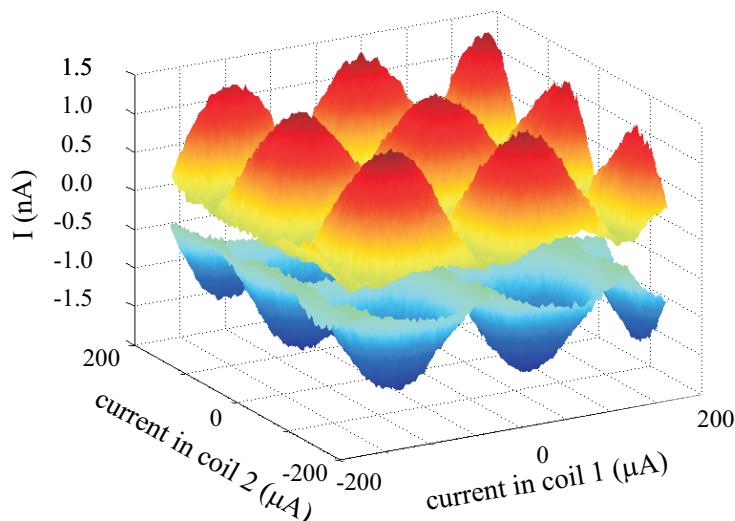symmetric. (c) Experimental setup for flux assisted pumping.

Figure 4.10: The measured current through the device as a function of applied *dc* currents in the two input coils. The data is presented for two different bias voltages corresponding to supercurrent maxima at the positive and negative directions, respectively.

2D flux modulation: a pumping path

In the flux assisted pumping it is essential to know the values of mutual inductances and also the value of initial external flux. These were estimated based on measured 2D flux modulation map illustrated in Fig. 4.10. This was measured by applying a small bias voltage across the sample (the voltage at the maximum of the supercurrent peak) and by measuring the current with varying *dc* currents through the input coils. The map is measured at both positive and at negative supercurrent directions, and they are both presented in Fig. 4.10. It can be seen that the modulation picture is oriented almost perfectly in the axis directions, which indicates small cross-inductance.

The used parameter sequences were roughly like those illustrated in Fig. 4.8. The shape of the pulses was not optimized. The flux modulation amplitudes were estimated from the measured 2D modulation map in Fig. 4.10. The initial magnetic field was set accurately to correspond to a flux $= \Phi_0/2$ through the both *dc*-SQUIDs. The cross-inductance compensation between the coil currents was optimized by applying the flux sequences to the sample without gate signal and by minimizing the leakage current by tuning the value of the compensation.
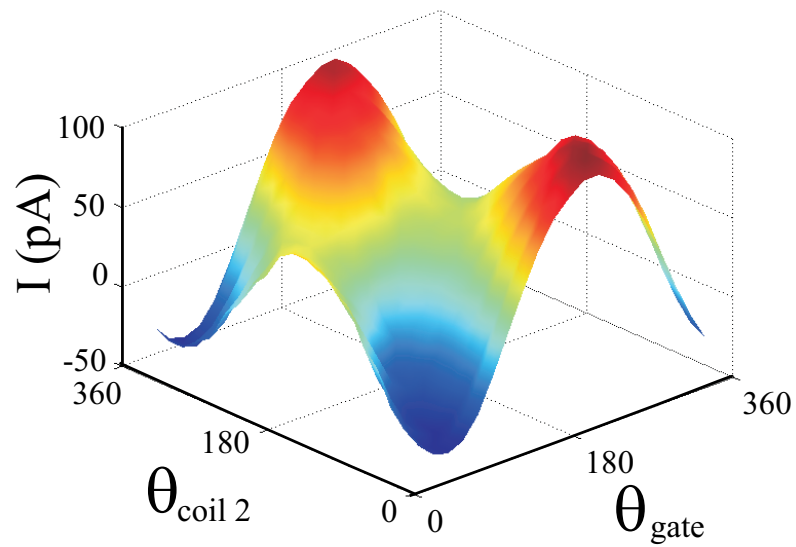
Figure 4.11: The measured current as a function of relative phase differences at the constant voltage of 250 μV with the 2 MHz pumping signal. The maximum and minimum of I present the corresponding optimal values of relative phases and at these points the value of the pumped current is maximized. The amplitude of the gate signal was set far over the adiabaticity limit (400e) for getting large signal for calibration purposes.
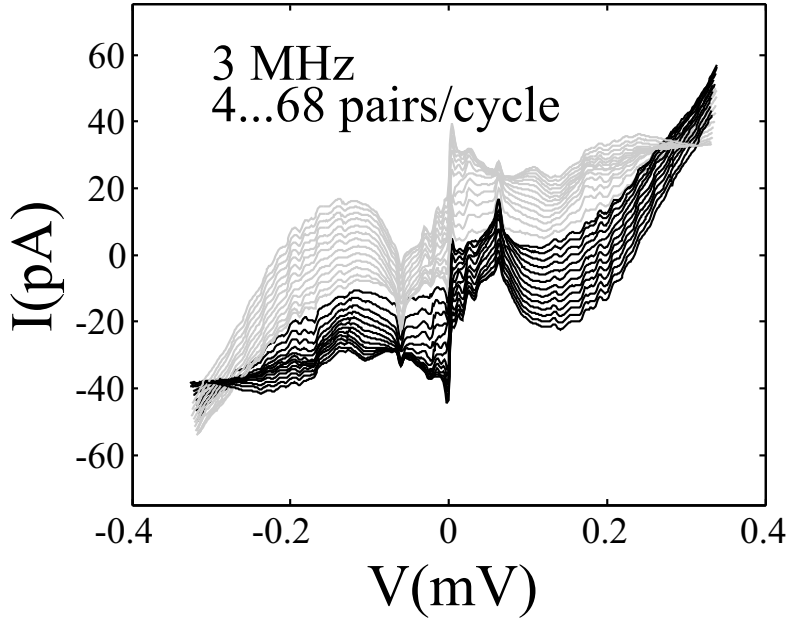
Figure 4.12:   The IV-characteristic of the flux assisted pump with 3 MHz pumping sequence and with different gate amplitudes between 3 and 68 pairs per pumping cycle. The black lines correspond to pumping in "backward" direction and the grey ones in "forward" direction.

The three signal generators were synchronized, but the initial relative phases between different devices were arbitrary. These were adjusted in the beginning of every pumping measurement and it was done by applying pumping signals to the sample and by measuring the current against the relative phases. The phase of the gate signal with respect to an arbitrary initial value is marked as θ_{gate} and that of the signal in coil 2 as $\theta_{\text{coil 2}}$. The phase of the signal in coil 1 was fixed. The results are presented in Fig. 4.11. The minimum and maximum of the current show the optimal choices of relative phases. In an example shown in Fig. 4.11 this is approximately $\theta_{\text{coil 2}} = 10^{\text{o}}$ for flux signal and the phases of the gate signals for pumping in "forward" and "backward" directions are $\theta_{\text{gate}}^{\text{forward}} = 200^{\text{o}}$ and $\theta_{\text{gate}}^{\text{backward}} = 20^{\text{o}}$, respectively. Note that a 180° phase shift in a gate signal changes the sign of the pumped current, as expected.

The results of the pumping experiment

Figure 4.12 presents the results of the flux assisted pumping experiment. Shown IV-characteristics are measured with 3 MHz frequency with various
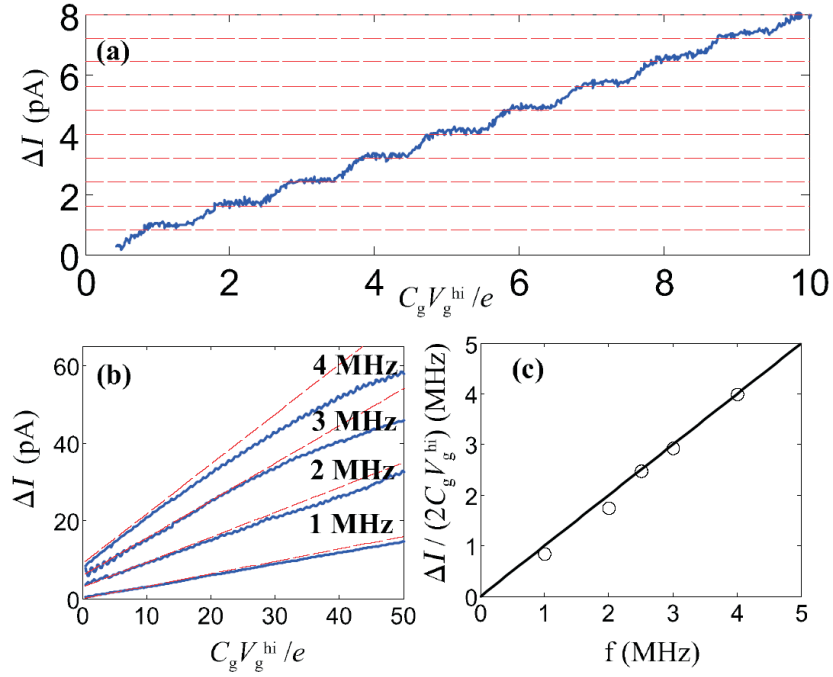
Figure 4.13: (a) Difference ΔI in current between "backward" and "forward" pumping directions as a function of the peak-to-peak amplitude of the gate signal keeping the low level of gate voltage at zero. The pumping frequency was 2.5 MHz and the bias voltage was around 10 μV. (b) ΔI with larger amplitude scale at various pumping frequencies. (c) The slopes for the linear fits to the pumping data of the previous figure (dashed lines) at the frequencies of the measurements. The solid line shows the expected ideal relation.

gate amplitudes corresponding from 3 to 68 Cooper pairs per pumping cycle. The black lines are measured with the pumping in "backward" direction and gray lines in the "forward" direction. The measured IV-characteristic also shows undesired *leakage* under the pumped current (current is not zero without pumping), which should be subtracted before more detailed analysis. The subtraction was made by calculating the current difference ΔI between "forward" and "backward" pumping directions and this is presented in Fig. 4.13. In contrast to the *leakage* current, the sign of the *pumped* current is different for different pumping directions. The current ΔI is thus twice the expected pumping current without a leakage. Figure 4.13 (a) presents ΔI on a smaller and (b) on a larger gate voltage amplitude scale. We made linear fits to the currents in Fig. 4.13 (b) and the slopes are given in (c).

4.3.2   Discussion

The results of the measurement on flux assisted pumping were very promising. The direction of the pumped current was set by the pumping sequence and not by the bias voltage unlike in the case of the double island pump. The measured currents at various pumping frequencies in Fig. 4.13 (b) are following the linear trend at small amplitudes, as expected. The fitted slopes of the linear dependencies in (b) are shown in Fig. 4.13 (c) together with an ideal frequency dependence. The agreement between the fitted values (open circles) and the theoretical black solid line is satisfactory. Figure 4.13 (b) indicates that the pumped current lacks below the expectation with increasing gate signal amplitude and frequency, but up to 10 pairs per pumping cycle the agreement is satisfactory also at the pumping frequency of 4 MHz.

The pumped current should increase in $2ef$ steps with increasing gate signal amplitude. Here f is the pumping frequency. Each time when gate charge passes one more degeneracy point, the number of Cooper pairs pumped per one cycle is increasing by one. The current ΔI exhibits a step like behaviour as shown in Fig. 4.13 (a). The separation between horizontal dashed lines in Fig. 4.13 (a) corresponds to a current of $2ef$ and we can see that the step height is very close to it. However, the presented current ΔI should be *twice* the pumped current and thus the expected height should be $4ef$. Steps should also occur at $2e$ intervals in the gate charge instead of the measured $1e$. Nonetheless, the main charge carriers are still claimed to be Cooper pairs. One argument in favour of this conclusion is that tuning the Josephson coupling plays such an important role in results of pumping, and also because the pumped current changes sign when the phase of the gate signal was shifted 180º with respect to *flux signals*. The parity changes due to non-equilibrium quasiparticles over time scales longer than the inverse pumping frequency but much shorter than the current averaging time would produce the observed averaged structure of two $2e$-periodic staircases that are shifted by e in the gate charge. This is probably what occurs, and these observations are consistent with those on the double island pump presented in the previous Section.

Measured IV-characteristics show strong leakage in addition to the pumped current. Close to zero voltage the leakage current presents peaks, which are due to a residual coupling across the device. The most probable explanation is that the junctions in the dc-SQUID were not identical. However, the strong leakage far from zero bias could not be explained by tunneling of Cooper pairs and thus the quasiparticles were probably also playing a role.

4.4   Summary

Observations on both types of Cooper pair pumps indicate existence of non-equilibrium quasiparticles. However, the experimental results indicated that the main charge carriers are Cooper pairs. The earlier assumption has been that the quasiparticles are tunneling completely stochastically. Surprisingly, the agreement between the theory and the measured current indicates that this is not the case. When operating close to a triply degenerate node of the double island pump the quasiparticle tunneling seems to have a minor effect. This is a contradiction with the measured honeycomb, which was an average over all distinguishable quasiparticle configurations and would thus indicate extensive quasiparticle tunneling. In [PIV] this was successfully explained by the model, which suggests that if the quasiparticles have freedom to move, they will arrange themselves in a configuration, which will maximize the supercurrent.

The value of the pumped current in a double island pump followed the relation $I = 2ef$ at low frequencies. Yet, the sign of the current was given by the bias voltage. The measured sample also exhibited strong leakage in addition to the pumped current. Both failures were explained by extensive cotunneling due to large E_J. In the Cooper pair pump with bare Josephson junctions the high pumping speed and large pumping accuracy are contradicting requirements. The Landau-Zener limit would favor strong Josephson coupling E_J, which yields a large cotunneling rate and large leakage current.

The most remarkable benefit of the flux assisted pump is that E_J is temporarily large only when necessary, and thus leakage errors can be avoided at least in principle. Yet, the experiments on flux assisted pump suffered from leakage current because the Josephson coupling could not be tuned all the way to zero due to the asymmetry of junctions in the dc-SQUIDs. The measurements demonstrated, however, the idea, and the current pumped compared favourable with the prediction. The idea of the flux assisted pumping also scales to longer arrays, which in principle should be more insensitive to residual E_J. Therefore future studies should probably be focused in this direction.

Chapter 5

Thermometer based on NIS tunnel junctions

Symmetric Superconductor - Insulator - Normal metal - Insulator - Superconductor tunnel junction pairs, SINIS structures, are known to have interesting applications in solid-state cooling and thermometry [67, 68]. For example in bolometric radiation sensor applications SINIS structure is a very promising temperature sensor. This Chapter presents experimental studies, which showed that a SINIS structure can be used as a sensitive thermometer up to MHz frequency range and that the response time is limited by electron-phonon scattering rate [PVI, PVII]. In this Thesis a novel technique for direct electron-phonon relaxation time measurement is introduced. Earlier studies of the electron-phonon scattering rate were done by dc measurements, where one has to use many material dependent parameters and assumptions [69, 10, 68].

5.1 Temperature measurement using symmetric SINIS structures

The tunneling current in a NIS junction, Eq. (2.10), is strongly temperature dependent at subgab voltages $V < \Delta_{\mathrm{BCS}}/e$ and due to this it can be used as a sensitive thermometer. With the help of Eq. (2.11) one can write the sensitivity $S_T = dV/dT_e$ at a fixed current bias into a form

$$\frac{dV}{dT_e} \simeq \frac{k_{\mathrm{B}}}{e} \ln[e^{(eV-\Delta)/k_{\mathrm{B}}T_e}], \tag{5.1}$$

where T_e is the electronic temperature of the normal metal.

The steady state temperature of the thermometer due to applied constant heating power $\dot{Q}_{HEAT}$ can be written as $T = R_{\text{th}}\dot{Q}_{HEAT} + T_0$. Here thermal resistance $R_{\text{th}}(T) = 1/G_{\text{th}}(T)$ gives the thermal coupling between the environment and the sensing element and it sets the limit for the power sensitivity in bolometric applications. The initial temperature without heating power is T_0. However, analogously to electrical circuits, with alternating heating the amplitude of the temperature change is limited by the heat capacity of the sensing element $C_s(T)$ via equation $\dot{Q} = C_s(T)\dot{T}$.
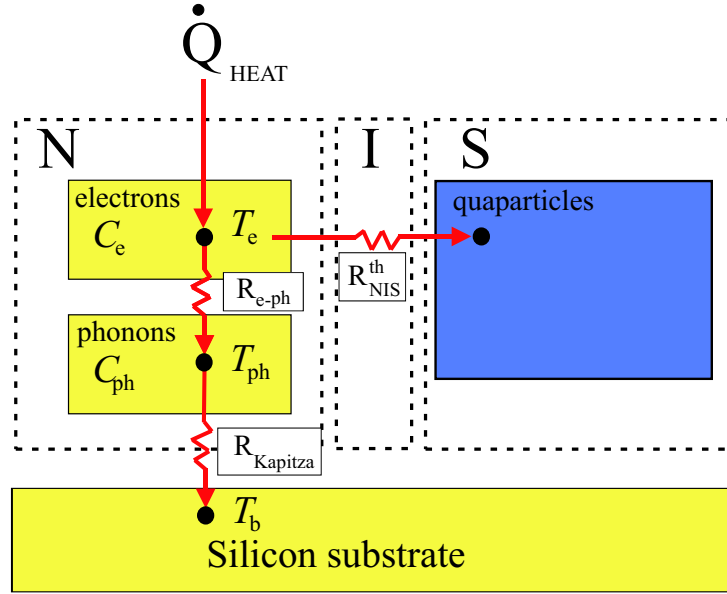

Figure 5.1: A block diagram of heat paths in a SINIS thermometer structure. Here C_e is the electronic heat capacity on the island, C_{ph} is the heat capacity of the phonons and $\dot{Q}_{\text{HEAT}}$ is the incoming heating power. $R_{\text{e-ph}}$ is the thermal resistance between electrons and phonons. The thermal resistance between the phonons in the island and the phonons in the substrate, R_{Kapitza}, is assumed to be small.

The normal metal island of the SINIS structure can be divided into two interacting subsystems, into electrons and phonons. Figure 5.1 presents the block diagram of possible heat paths of the electron gas. The thermal coupling directly through the NIS junctions is usually very weak and thus the dominating heat path is between electrons and phonons. The thermal resistance between the phonons in the island and the phonons in the substrate, R_{Kapitza}, is assumed to be negligible.

In a SINIS structure two NIS junctions with common normal metal electrode are connected in series. An important advantage of the symmetric

SINIS structure for bolometric purposes is that the normal metal island can be mesoscopic, and thus the heat capacity of the sensing element can be small. Smaller size of the sensing element yields a weaker thermal coupling to the environment.

5.1.1 Response time of a SINIS thermometer

The speed of the thermometer is usually limited by the thermal relaxation time of the sensing element. This can be written as

$$\tau_{\text{th}}(T) = R_{\text{th}}(T)C_s(T). \tag{5.2}$$

In the case of a SINIS thermometer, the response time is given as

$$\tau = \left(\frac{\partial \dot{Q}_{\text{e-ph}}(T_e, T_{ph})}{\partial T_e} \right)^{-1} C_e, \tag{5.3}$$

where $C_e = \Omega\gamma T_e$ is the electronic heat capacity (γ is the Sommerfield constant), and the $\dot{Q}_{\text{e-ph}}(T_e, T_{ph})$ is the heat current between electrons and phonons. T_{ph} is the temperature of the phonons. In three dimensions the e-ph cooling power can be written as [69]

$$\dot{Q}_{\text{e-ph}}(T_e) = \Sigma\Omega(T_e^5 - T_{ph}^5), \tag{5.4}$$

where Σ is a material dependent parameter of the order of 10^9 W/K^{5}m^3 and Ω is the volume of the normal metal island. Consequently the response time, $i.e.$, the electron-phonon relaxation time, can be written finally in a form

$$\tau_{\text{e-ph}} = \frac{\gamma}{5\Sigma}T_e^{-3} = a^*T^{-3}, \tag{5.5}$$

which is independent of the volume of the normal metal island. Here a^* is experimentally determined fitting parameter. The relaxation time is directly proportional to the average e-ph scattering rate and it does not depend on other material or geometric parameters. It is a weighted average of electron-phonon relaxation time over energy [69].

5.2 Experimental setup and measured samples

The technique of a direct relaxation time measurements is based on the non-linear temperature dependence of the electron-phonon coupling, see Eq.

(5.4). The temperature of the normal metal island is measured at low frequency even though it is measured against the applied frequency of Joule heating. When the heating frequency exceed the natural electron-phonon relaxation rate, the time averaged temperature is also affected due to non-linearity. With sinusoidal heating power at frequencies below the cut-off frequency $f_c = 1/2\pi\tau_{\mathrm{e-ph}}$ the measured averaged temperature is *the time average of the oscillating strongly non-sinusoidal temperature $T_e(t)$*. Above the cut-off frequency the electronic temperature does not have time to follow heating oscillations anymore and thus the measured temperature corresponds to T_e with *time averaged heating power*. This temperature differs from time averaged temperature at low heating frequencies due to non-linear thermal coupling. Note that we are not able to measure electronic temperature at high frequencies directly due to limited bandwidth of the voltage measurement. This is limited by the RC time constant of the circuit, where R is the resistance of the NIS tunnel junction ($\approx 10\,\mathrm{k\Omega}$) and C is the capacitance of the measuring lines, usually a few hundred pF.
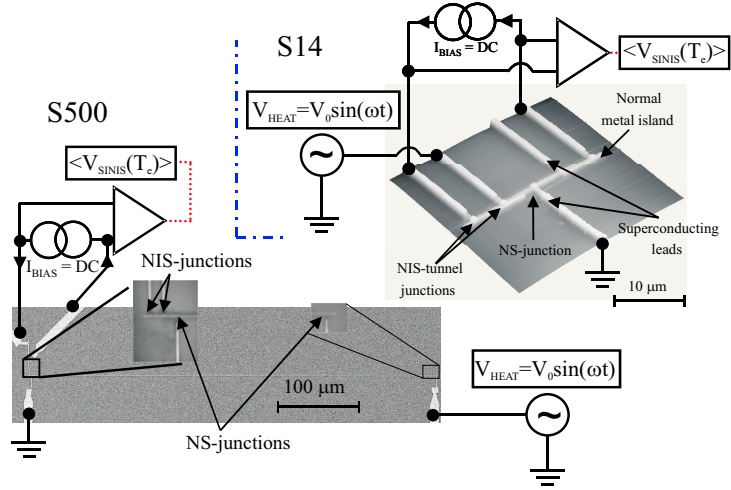

Figure 5.2: The micrographs of the sample geometries and experimental setup used for direct electron-phonon coupling measurement.

Figure 5.2 presents micrographs of the sample S14 with 14 μm long copper island and of the sample S500 with 500 μm island. In both cases the width of the island was about 0.5 μm and thickness of the copper film was about 50 nm. The SINIS structures had copper normal metal islands and the superconducting leads were made out of aluminum. The samples were fabricated by using three angle evaporation and the NIS tunnel junctions were formed by room temperature oxidation after the first evaporation of alu-

minum. The samples have also direct metallic Normal metal-Superconductor (NS) contacts to the copper island. The NS contact is providing a low resistance electrical contact to normal metal, but the heat leak through it is negligible due to Andreev reflection. The good electrical contact is needed for direct grounding of the island. This prevents alternating current to heat the thermometer NIS junctions at high frequencies.

The copper island of S500 was heated by Joule heating by applying an *ac* voltage between two NS junctions, whereas in the sample S14 a NIS junction served as the heating element. The electrons were able to be heated in the frequency range from zero up to few MHz and the upper limit was given by the bandwidth of the the electrical wiring of the cryostat. The measured voltage was amplified by using a DL-Instruments 1201 low-noise preamplifier, and a DL-Instruments 1211 pre-amplifier was used as a current amplifier. All measurements were done in a $He^3 - He^4$ dilution refrigerator, whose minimum temperature was around 50 mK.
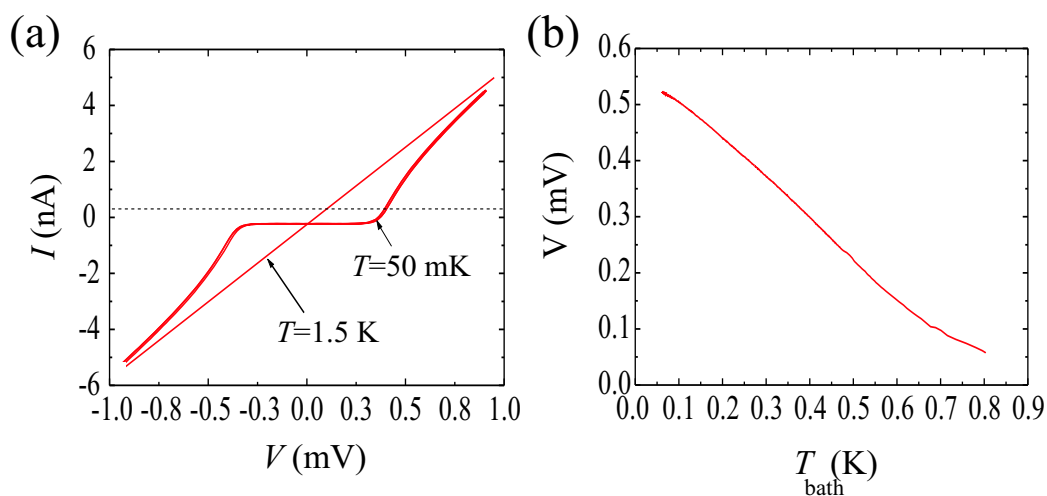
5.3   Results

Figure 5.3: (a) *IV*-characteristics of a SINIS structure at $T_e \approx 60$ mK and $T_e \approx 1.5$ K ($R_T \approx 10$ kΩ). (b) The voltage across the SINIS structure at different temperatures at a fixed current bias, which is indicated by a dashed line in (a).

Figure 5.3 (a) illustrates examples of the measured *IV*-characteristics at two different temperatures. In Fig. 5.3 (b) we show the voltage as a function of temperature at a small fixed current bias presented by a dashed line in

(a). Similar $V(T_e)$ calibration curve was measured at the beginning of all measurements below. The SINIS thermometers were calibrated against a ruthenium oxide (RuO) thermometer by slowly sweeping the bath temperature. The measured sensitivity in Fig. 5.3 (b) is approximately 1 μV/mK.

The measurements with *ac* heating were done either by sweeping heating power with fixed frequency or by keeping the heating power constant and sweeping frequency. The results are presented in Fig. 5.4 and in Fig. 5.6.
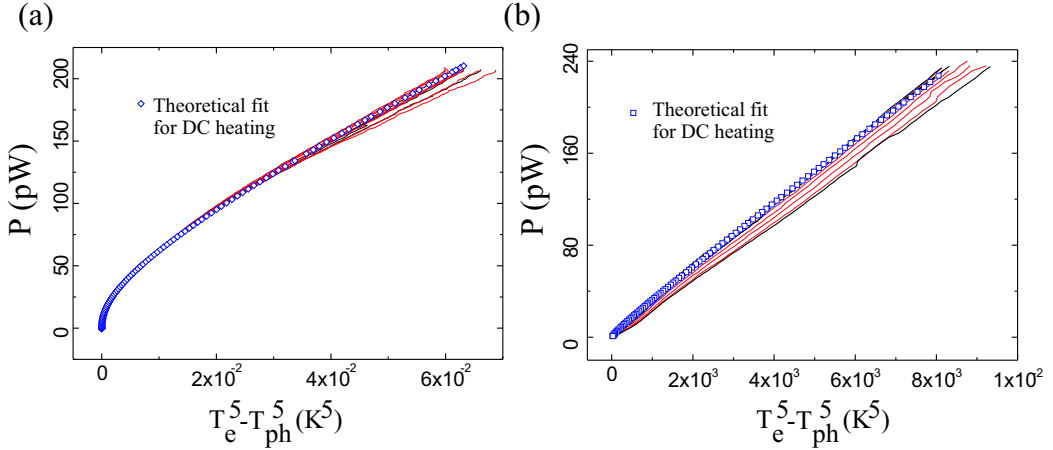

Figure 5.4: Heating power as a function of electronic temperature of the copper island at different heating frequencies between *dc* and 2 MHz. (a) Results on the sample S14 and (b) on the sample S500. The uppermost curves were measured by constant current heating (*dc*) whereas those deviating most from these were measured at 2 MHz.

5.3.1 Electronic temperature under low frequency heating

Figure 5.4 presents heating power as a function of the measured electronic temperature at different heating frequencies between *dc* and 2 MHz. The results of the *dc* heating measurements on the sample S500 in Fig. 5.4 (b) follow the power law of Eq. (5.4). However, the temperature dependence of the results on sample S14 presented in Fig. 5.4 (a) differs from that of Eg. (5.4). The probable reason is that at the low temperatures the e-ph coupling is very weak and thus in sample with small volumes, also other heat paths should be taken into account. For the sample S14 with 14 μm copper island the total cooling power of the Cu island can be descibed reasonably

well as

$$\dot{Q} = \dot{Q}_{\text{e-ph}}(T_e) + \dot{Q}_{\text{NS}}(T_e), \tag{5.6}$$

where the two terms are due to cooling by electron-phonon coupling and due to heat leak through the non-ideal NS junction. In [PVI] we concluded that this heat flow can be approximated as

$$\dot{Q} = \Sigma\Omega(T_e^5 - T_{ph}^5) + \frac{1}{R_m^{\text{eff}}e^2}\frac{\pi^2}{3}k_B^2(T_e^2 - T_{ph}^2), \tag{5.7}$$

where R_m^{eff} is the effective normal state resistance of the NS contact, which includes coefficients of Andreev and normal reflections as well. The model also assumes that the temperature of superconducting electrodes equals to that of phonons on the island, $T_S = T_{ph}$. Figure 5.4 presents the fitted Eq. (5.7) for the lowest heating frequency using two free parameters Σ and R_m^{eff}. The best fit gives $\Sigma = 5.0 \times 10^9$ nW/K^{5}m^3 and $R_m^{\text{eff}} = 50$ Ω for sample S14 and $\Sigma = 3.5 \times 10^9$ nW/K^{5}m^3 and $R_m^{\text{eff}} = 150$ Ω for S500.

5.3.2 Electronic temperature under high frequency heating

Figure 5.4 shows at with higher heating frequencies the electronic temperature starts to deviate from that in the low frequency data. Figs. 5.5 and 5.6 show the temperature as a function of the heating frequency at various heating powers. The data presented in Fig. 5.5 is the same as that in Fig. 5.4.

The f-dependence was modeled using a first order filter form (solid lines in Fig. 5.5). These fitted cut-off frequencies are shown in Fig. 5.7 as a function of the electron temperature. The solid line in Fig. 5.7 is the cut-off frequency $f_c = 1/2\pi\tau_{e-ph}$, where τ_{e-ph} is given by Eq. (5.5), with fitted value $1/a^* = \frac{5}{2\pi}\Sigma/\gamma = 0.0135$ Hz/mK^3. The same theoretical line is presented also in Fig. 5.5. The dashed line in Fig. 5.7 is calculated by using the literature value $\gamma = 0.688$ mJ/mol K^2 [70] and the fitted coupling constant $\Sigma = 3.5 \times 10^9$ nW/K^{5}m^3 for the dc heating measurement.

5.4 Discussion and conclusions

A thermometer based on NIS junctions has proven to work as an ultrasensitive thermometer up to MHz frequencies. The performance of the thermometer is limited by the e-ph coupling in many respects: the ultimate response time is given by the e-ph scattering rate, but on the other hand for bolometric purposes the sensitivity is limited by this heat path as well.
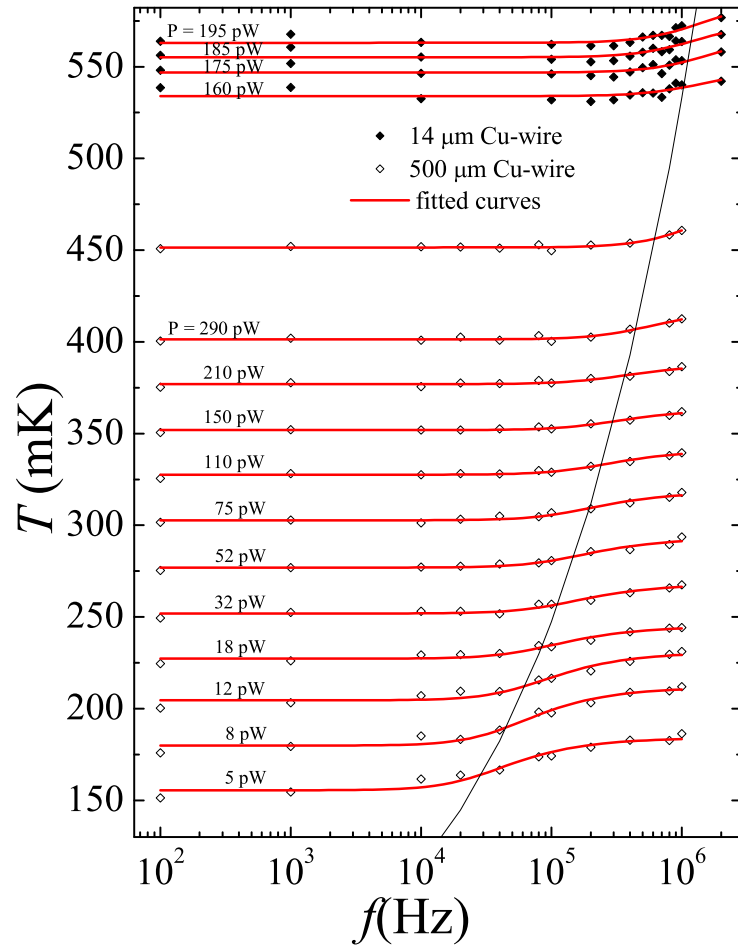
Figure 5.5: The electronic temperature at different *ac* heating frequencies with constant levels of heating power. The data is the same as in Fig. 5.4. The solid line is the theoretical cut-off frequency (discussed in the text).
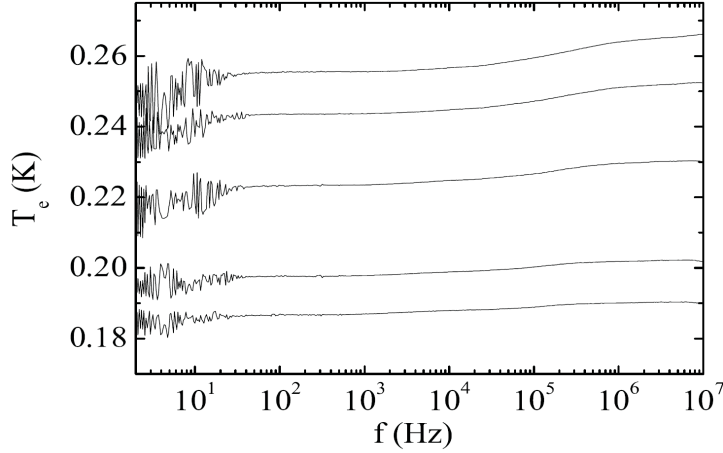
Figure 5.6: The measured electronic temperature at different *ac* heating frequencies at various constant heating powers. The highest average temperature (the uppermost curve) corresponds largest heating power.

The fitted values of the electron coupling constant agree fairly well with the earlier measured value $\Sigma = 4 \times 10^9$ nW/K^{5}m^3 [68]. The observations on the sample with a small normal metal island indicate that the NS contacts are *leaking* thermally. This is probably because the NS contacts are not perfect Andreev mirrors.

A method to measure the electron-phonon relaxation time directly has been demonstrated for the first time. This relaxation time is directly proportional to the average e-ph scattering rate and it does not depend on material or geometry parameters. The measured $\tau_{\mathrm{e-ph}}$ agrees well with the one calculated by using a fitted Σ and the literature value for γ. The temperature dependence of the $\tau_{\mathrm{e-ph}}$ was close to T^{-3}, as expected. Due to strong temperature dependence, the relaxation time is already in the range of milliseconds at temperatures of the order of 10 mK, even though the relaxation time is well below 1 μs at temperatures of few hundred mK.

In publication [PVII] we discuss small samples at low temperatures where the power law Eq. (5.4) does not hold anymore. This is most likely a strongly sample dependent phenomenon, and it is thus not discussed in this overview of the Thesis.
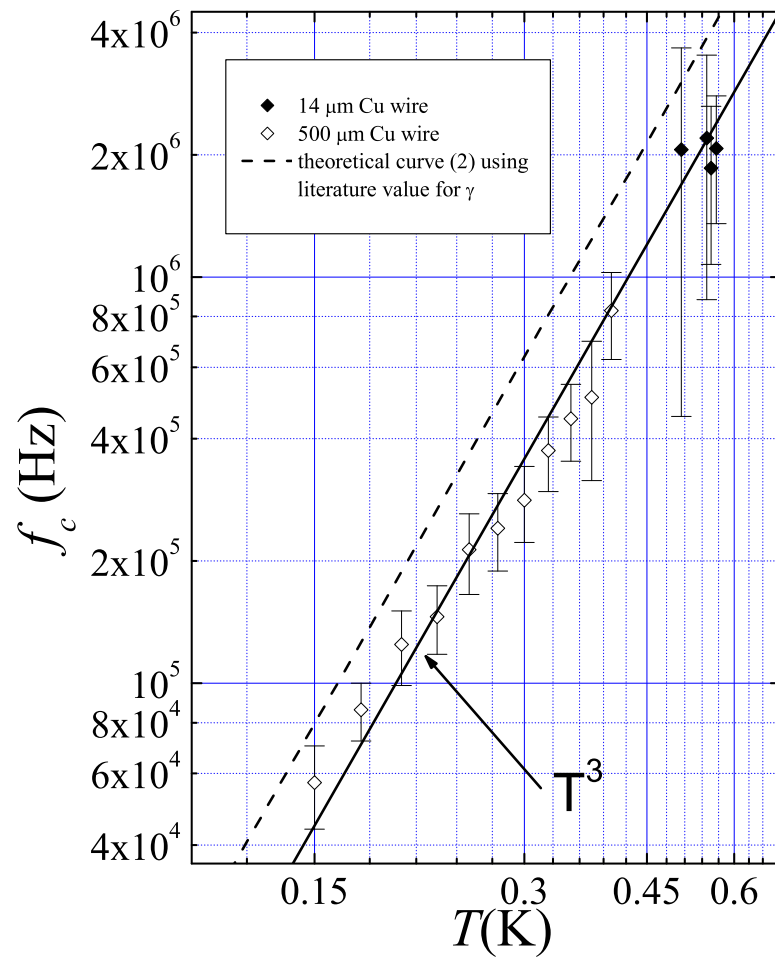
Figure 5.7: The thermal cut-off frequency as a function of temperature of the copper island. Frequency is independent of sample size.

Chapter 6

General discussion and summary

In this Thesis four mesoscopic superconducting tunnel junction devices were investigated: a Josephson junction ammeter, a double island Cooper pair pump, a flux assisted Cooper pair pump and a thermometer based on NIS junctions. These devices have been realized and their operation and limitations have been investigated experimentally. Furthermore, during the work possibilities to improve the performance of these devices have also been explored.

We conclude in Chapter 3 that the current sensitivity of the Josephson junction ammeter is increasing with decreasing critical current. The main limitation of the ammeter was that with increasing sensitivity the negative effects due to dissipation start to dominate. We found that in our experimental set-up Josephson junctions with 100 nA critical current still have suitable properties for current detector purposes. This yields a sensitivity of around 22 %/nA with 100 fF junction capacitance. Here sensitivity is defined as (maximum) change of escape probability per unit current. Tanaka *et al.* [34] have used weak coupling dc-SQUID for detecting the quantum state of the superconducting quantum bit and in their experiment they also observed that with critical currents below ~ 100 nA the behaviour of the detector changed. Above this limit their current sensitivity was about the same as what we observed. However, our observations indicate that an inductive environment would provide a way to decrease the acceptable critical current further and thus increase the maximum sensitivity. On the other hand, in the "Quantronium" experiment Vion *et al.* [12] used Josephson junction ammeter with sufficiently large 1.17 μA critical current, but they increase current sensitivity by increasing junction shunting capacitance with an external on-chip capacitor. Their maximum sensitivity was around 10 %/nA in MQT regime.

In Chapter 3 the Josephson junction was also demonstrated as a shot-noise detector, and it was concluded that this kind of a device could probably be made into an absolute on-chip detector of Fano-factors and noise in general.

The measured double island Cooper pair pump, CPP, introduced a frequency dependent current with a value close to the expected one at low pumping frequencies. The drawback in the measurements was that the direction of the pumped current was set by the bias voltage. On the contrary, in their pioneering douple island Cooper pair pump experiment Geerligs *et al.* [60] were able to pump charge against the bias voltage as well. One possible reason for this difference is that our sample had much larger Josephson coupling energy E_J than what the sample in their experiment had. The double island pump measured in this Thesis suffered from strong cotunneling, leakage and other uncontrollable processes probably indeed due to sufficiently large E_J. Large current can be achieved with strong Josephson coupling E_J, which cannot, however, be allowed in these devices. It is thus unlikely that a conventional CPP would provide a current standard in the future, and more complex systems, like devices with dissipative environment [61] or with tunable Josephson coupling [62], are needed.

The results of the measurement on flux assisted pumping were indeed very promising and the studied device was able to produce pumped currents of around 0.1 nA with reasonable accuracy despite of several non-idealities. Future generations of such devices, with longer *dc*-SQUID arrays, will probably introduce a true candidate of a current standard. The most promising device for this purpose, until now, is the seven junction single electron pump [55]. However, in this case the maximum pumped current is only few pA, which is much less than what our present flux assisted pump experiment demonstrated.

A thermometer based on NIS tunnel junctions is a very promising temperature sensor for bolometric radiation sensor applications [71]. The measurements showed that it can be used as a sensitive thermometer up to MHz frequencies range and that its response time is limited by the electron-phonon scattering rate. In this Thesis a novel technique to measure this scattering rate directly was developed for the first time. There do not exist direct scattering rate experiments besides the ours presented in this Thesis, but the measured rate values are in good agreement with the results of the earlier indirect measurements [68].

The devices presented in this Thesis make use of phenomena based on quantum mechanics and their operation could not be explained by classical physics. They have many possible individual scientific applications in the near future. These particular devices will probably never be in wide everyday use, but they present a step towards nanoelectronic devices.

References

[1] J. Singh, *Semiconductor Optoelectronics: Physics and Technology*, (McGraw-Hill, Singapore, 1995).

[2] L.E. Ballentine, *Quantum Mechanics: A Modern Development*, (World Scientific, Singapore, 1998).

[3] S. Franssila, *Introduction to Microfabrication*, (John Wiley & Sons Ltd., West Sussex, England, 2004).

[4] M.A. Nielsen and I.L. Chuang, *Quantum Computation and Quantum Information*, (Cambridge University Press, Cambridge, England, 2000).

[5] M. Tinkham, *Introduction to superconductivity, 2nd ed.* (McGraw-Hill, New York, 1996).

[6] G.-L. Ingold and Yu. V. Nazarov, in *Single Charge Tunneling: Coulomb Blockage Phenomena In Nanostructures*, edited by H. Grabert, M.H. Devoret (Plenum Press, New York, 1992), p. 21.

[7] M.T. Tuominen *et al.*, Phys. Rev. Lett. **69**, 1997 (1992).

[8] V. Ambegaokar and A. Baratoff, Phys. Rev. Lett. **10**, 486 (1963).

[9] F. Balestro, J. Claudon, J.P. Pekola, and O. Buisson, Phys. Rev. Lett. **91**, 158301 (2003).

[10] M.M. Leivo, Doctoral thesis, University of Jyväskylä (1999).

[11] G.J. Dolan, Appl. Phys. Lett. **31**, 337 (1977).

[12] D. Vion *et al.*, Science **296**, 886 (2002).

[13] S. Saito, M. Thorwart, H. Tanaka, M. Ueda, H. Nakano, K. Semba, and H. Takayanagi, Phys. Rev. Lett. **93**, 037001 (2004).

[14] J. Tobiska and Yu. V. Nazarov, Phys. Rev. Lett. **93**, 106801 (2004).

[15] J.P. Pekola, Phys. Rev. Lett. **93**, 206601 (2004).

[16] D. Vion *et al.*, Phys. Rev. Lett. **77**, 3435 (1996).

[17] J. Sjöstrand *et al.*, cond-mat/0406510 (2004).

[18] A. Franz *et al.*, Phys. Rev. B **69**, 014506 (2004).

[19] J.M. Martinis and R.L. Kautz, Phys. Rev. Lett. **63**, 1507 (1989).

[20] R.L. Kautz and J.M. Martinis, Phys. Rev. B **42**, 9903 (1990).

[21] U. Weiss, *Quantum Dissipative Systems*, (World Scientific, Singapore, 1999), 2nd ed..

[22] O. Buisson, F. Balestro, J.P. Pekola, and F.W.J. Hekking, Phys. Rev. Lett. **90**, 238304 (2003).

[23] O.Buisson and F.W.J. Hekking, in *Macroscopic Quantum Coherence and Quantum Computing*, edited by D.V. Averin, B. Ruggiero, and P. Silvestrini (Kluwer, New York, 2001), p. 137.

[24] R. Fazio, F.W.J. Hekking, and J.P. Pekola, Phys. Rev. B **68**, 054510 (2003).

[25] G.-L. Ingold, H. Grabert, and U. Eberhardt, Phys. Rev. B **50**, 395 (1994).

[26] A.I. Larkin and Yu.N. Ovchinnikov, Zh. Eksp. Teor. Fiz **91**, 318 (1986); A.I. Larkin and Yu.N. Ovchinnikov, Sov. Phys. JETP **64**, 185 (1987).

[27] A.I. Larkin and Yu.N. Ovchinnikov, Zh. Eksp. Teor. Fiz **87**, 1842 (1984); A.I. Larkin and Yu.N. Ovchinnikov, Sov. Phys. JETP **60**, 1060 (1984).

[28] A.B. Zorin, Rev. Sci. Instrum. **66**, 4296 (1995).

[29] P. Joyez *et al.*, J. of Superconductivity **12**, No. 6, 757 (1999).

[30] J. Claudon, Master's Thesis, CNRS, Grenoble, France (2002).

[31] A. Steinbach *et al.*, Phys. Rev. Lett. **87**, 137003 (2003).

[32] A. Cottet *et al.*, Physica C **367**, 197 (2002).

[33] J.M. Martinis, S. Nam, J. Aumentado, and C. Urbina, Phys. Rev. Lett. **89**, 117901 (2002).

[34] H. Tanaka, S. Saito, H. Nakano, K. Semba, cond-mat/0407299.

[35] P. Silvestrini, V.G. Palmieri, B. Ruggiero, and M. Russo, Phys. Rev. Lett. **79**, 3046 (1997).

[36] V. Lefevre-Seguin, E. Turlot, C. Urbina, D. Esteve, and M.H. Devoret, Phys. Rev. B **46**, 5507 (1992).

[37] J. Clarke, A. N. Cleland, M. Devoret, D. Esteve, and J.M. Martinis, Science **239**, 992 (1982).

[38] S. Washbourn , R.A. Webb, R.F. Voss, and S.M. Faris, Phys. Rev. Lett. **54**, 2712 (1985).

[39] M. Devoret *et al.*, Phys. Rev. Lett. **53**, 1260 (1984).

[40] P. Silvestrini *et al.*, Phys. Rev. Lett. **60**, 844 (1988).

[41] M. Castellano, R. Leoni, and R. Torreoli, J. Appl. Phys. **80**, 2922 (1996).

[42] Y. Yu, S. Han, X. Chu, S. Chu and Z. Wang, Science **296**, 889 (2002).

[43] M. Devoret, D. Esteve, J. M. Martinis, Phys. Rev. B **36**, 58 (1987).

[44] A.N. Cleland, J.M. Martinis, and J. Clarke, Phys. Rev. B **37**, 5950 (1988).

[45] J.M. Martinis, M. Devoret, and J. Clarke, Phys. Rev. Lett. **55**, 1543 (1985).

[46] K. Segall *et al.*, Phys. Rev. B **67**, 220506 (2003).

[47] D.S. Crankshaw *et al.*, Phys. Rev. B **69**, 144518 (2004).

[48] B. Ruggiero *et al.*, Phys. Rev. B **57**, 134 (1998).

[49] C. Cosmelli *et al.*, Phys. Rev. Lett. **82**, 5357 (1999).

[50] B. Ruggiero *et al.*, Phys. Rev. B **59**, 177 (1999).

[51] P.A. Warburton *et al.*, Phys. Rev. B **67**, 184513 (2003).

[52] Y.M. Blanter and M. Büttiker, Physics Reports **336**, 1 (2000).

[53] K.K. Likharev and A.B. Zorin, J. Low Temp. Phys. **59**, 347 (1985).

[54] V. I. Talyanskii *et al.*, Phys. Rev. B **56**, 15180 (1997).

[55] M.W. Keller, J.M. Martinis, N.M. Zimmerman, and A.H. Steinbach, Appl. Phys. Lett. **69**, 1804 (1996).

[56] J.M. Ziman, *Principles of the theory of Solids*, (Cambridge University Press, Cambridge, England, 1964).

[57] J. Delahaye *et al.*, Science **299**, 1045 (2003).

[58] J.P. Pekola, J.J. Toppari, M. Aunola, M.T. Savolainen, and D.V. Averin, Phys. Rev. B **60**, R9931 (1999).

[59] M. Aunola, J.J. Toppari, and J.P. Pekola, Phys. Rev. B **62**, 1296 (2000).

[60] L.J. Geerligs *et al.*, Z. Phys. B **85**, 349 (1991).

[61] S.V. Lotkhov, S.A. Bogoslovsky, A.B. Zorin, and J. Niemeyer, Phys. Rev. Lett. **91**, 197002 (2003)

[62] A.O. Niskanen, J.P. Pekola, and H. Seppä, Phys. Rev. Lett. **91**, 177003 (2003).

[63] D. Vion, P.F. Orfila, P. Joyez, D. Esteve, and M.H. Devoret, J. Appl. Phys. **77**, 2519 (1995).

[64] K. Andersson, P. Delsing, and D. Haviland. Physica B **284**, 1816 (2000).

[65] L.J. Geerligs *et al.*, Phys. Rev. Lett. **64**, 2691 (1990).

[66] J.P. Pekola, K.P. Hirvi, J.P. Kauppinen, and M.A. Paalanen, Phys. Rev. Lett. **73**, 2903 (1994).

[67] M. Nahum, T.M. Eiles, and J.M. Martinis, Appl. Phys. Lett. **65**, 3123 (1994).

[68] M.M. Leivo, J.P. Pekola, and D.V. Averin, Appl. Phys. Lett. **68**, 1996 (1996).

[69] F.C. Wellstood, C. Urbina, and J. Clarke, Phys. Rev. B **49**, 5942 (1994).

[70] B.W. Roberts, *Properties of Selected Superconductive Materials*, NBS Technical Note 983, U.S Government Printing Office (1978).

[71] M. Tarasov, L. Kuzmin, E. Stepantsov, L. Agulo, A. Kalabukhov, M. Fominskii, Z. Ivanov, and T. Claesom, JETP Letters **79**, No. 6, 298 (2004).